Spatially resolved single-cell atlas of the lung in fatal Covid19 in an African population reveals a distinct cellular signature and an interferon gamma dominated response

James Nyirenda[1,2,3]*, Olympia Hardy[3,*], João Da Silva Filho[1,8]*, Vanessa Herder[6], Charalampos Attipa[1,3,5,7], Charles Ndovi[1,2,3], Memory Siwombo[9], Takondwa Namalima[9], Leticia Suwedi[3,10], Watipenge Nyasulu[1,3], Thokozile Ngulube[1,3], Deborah Nyirenda[3,10], Leonard Mvaya[3], Joseph Phiri[3], Dennis Chasweka[4], Chisomo Eneya[4], Chikondi Makwinja[4], Chisomo Phiri[4], Frank Ziwoya[4] , Abel Tembo[4], Kingsley Makwangwala[4] , Stanley Khoswe[4], Peter Banda[4,9], Ben Morton[3,10], Orla Hilton[11], Sarah Lawrence[12], Monique Freire dos Reis[13,14], Gisely Cardoso Melo[15], Marcus Vinicius Guimaraes de Lacerda[15,16,17], Fabio Trindade Maranhão Costa[18], Wuelton Marcelo Monteiro[14,15], Luiz Carlos de Lima Ferreira[14,15], Carla Johnson[1], Dagmara McGuinness[1], Kondwani Jambo[3,10], Michael Haley[22], Benjamin Kumwenda[4,] Massimo Palmarini[11], Kayla G. Barnes[5,19,20,+], Donna M. Denno[12,+], Wieger Voskuijl[21,4,9+] , Steve Kamiza[4,+] Kevin Couper[22,+] Matthias Marti[1,8,+] Thomas Otto[1,+], Christopher A. Moxon[1,2,3,9,+,**]

1. School of Infection and Immunity, University of Glasgow, Glasgow, UK.
2. Blantyre Malaria Project, Kamuzu University of Health Sciences, Blantyre, Malawi.
3. Malawi-Liverpool-Wellcome Programme, Kamuzu University of Health Sciences, Blantyre, Malawi.
4. Kamuzu University of Science of Health Sciences, Blantyre, Malawi.
5. Department of Vector Biology and Tropical Disease Biology, Liverpool School of Tropical Medicine, Liverpool, UK
6. Centre for Virus Research, School of Infection and Immunity, MRC-University of Glasgow
7. The Royal (Dick) School of Veterinary Studies and The Roslin Institute, University of Edinburgh, UK.
8. Universität Zürich, Institut für Parasitologie, Zurich, Switzerland.
9. Queen Elizabeth Central Hospital, Blantyre, Malawi
10. Clinical Sciences, Liverpool School of Tropical Medicine, Liverpool, UK.
11. Department of Infectious Diseases, Imperial College London, London, UK
12. Department of Global Health and Pediatrics, University of Washington, Seattle, USA.
13 Department of Education and Research, Oncology Control Centre of Amazonas State (FCECON), Manaus, Brazil
14 Postgraduate Program in Tropical Medicine, University of Amazonas State, Manaus, Brazil.
15 Tropical Medicine Foundation Dr. Heitor Vieira Dourado, Manaus, Brazil
16 Institute Leônidas & Maria Deane, Fiocruz, Manaus, Brazil
17 University of Texas Medical Branch, Galveston, USA
18 Department of Genetics, Evolution, Microbiology and Immunology, University of Campinas, Campinas, Brazil
19. Department of Immunology and Infectious Diseases, Harvard TH Chan School of Public Health, Boston, USA.
20. Broad Institute of MIT and Harvard, Cambridge, USA.
21. Department of Global Health, Amsterdam University Medical Centers, Amsterdam, Netherlands
22. Division of Immunology, Immunity to Infection & Respiratory Medicine, Faculty of Biology, Medicine & Health, The University of Manchester, Manchester, M13 9PT, United Kingdom

* These are first authors, these authors contributed equally
+ These are senior authors, these authors contributed equally
Correspondence to: matthias.marti@uzh.ch; ThomasDan.Otto@glasgow.ac.uk; Christopher.Moxon@glasgow.ac.uk
**Lead contact

ABSTRACT

Postmortem single-cell studies have transformed understanding of lower respiratory tract diseases (LRTD) including Covid19 but there is almost no data from African settings where HIV, malaria and other environmental exposures may affect disease pathobiology and treatment targets. We used histology and high-dimensional imaging to characterise fatal lung disease in Malawian adults with (n=9) and without (n=7) Covid19, and generated single-cell transcriptomics data from lung, blood and nasal cells. Data integration with other cohorts showed a conserved Covid19 histopathological signature, driven by contrasting immune and inflammatory mechanisms: in the Malawi cohort, by response to interferon-gamma (IFN-γ) in lung-resident alveolar macrophages, in USA, European and Asian cohorts by type I/III interferon responses, particularly in blood-derived monocytes. HIV status had minimal impact on histology or immunopathology. Our study provides data resources and highlights the importance of studying the cellular mechanisms of disease in underrepresented populations, indicating shared and distinct targets for treatment.

Introduction

There has been significant progress towards creation of a human cell atlas utilising scRNA-sequencing (scRNA-seq) and high-dimensional cellular imaging data[1,2]. The human cell atlas is transforming our understanding of cells and their states in health and disease and is rapidly becoming a major resource for the development of novel treatments and vaccines[3]. Yet, data within this atlas is heavily biased towards populations in the Northern hemisphere. Populations in sub–Saharan Africa (SSA) are particularly underrepresented[4]. Genetic and environmental factors may lead to important differences in cell development and cell-compositions in different organs, thus effecting cellular responses to diseases, vaccines and therapies[5,6]. Capturing data from SSA populations is critical to assure that everyone can benefit from the treatment advances derived from the human cell atlas.

Immunomodulation plays a critical role in Covid19 outcomes. Single-cell data from lung tissue facilitated identification of specific immunomodulatory targets[3,7-12]. Apart from our high-dimensional imaging study from a Brazilian cohort[13] these data are, thus far, exclusively from populations in Northern hemisphere, similar to most clinical trial data validating their efficacy. For future waves or epidemics of SARS-CoV2 or related viruses, this knowledge gap needs to be addressed. Indeed, given minimal intensive care, the benefit of preventing progression to or deterioration from severe disease by immunomodulation is even more important in SSA. While immunomodulatory therapies can be lifesaving, they can also be harmful[14]. Immunomodulation has focused on two opposing strategies: augmenting the inflammatory response to aid viral clearance or attenuating inflammatory response to

reduce pathogenic hyperinflammation. Extensive studies in northern hemisphere cohorts have established that, by the time patients present with life threatening illness, viral loads are declining, hyperinflammation generally predominates and thus anti-inflammatory interventions are more effective[14,15]. Given evidence that repeated exposure to malaria and other parasitic infections can induce immune tolerance[16-18], we hypothesised that the balance may be different in patients in SSA where these infections are more prevalent. While sometimes this clinical context may be protective, in those who progress to severe disease, a tolerance-skewed response might blunt immune-mediated viral clearance, leading to a more viral-driven pathology. However, the reverse is also possible. High pathogen exposure can induce an accelerated inflammatory response on re-exposure to pathogens[5]. Either scenario might impact cellular responses driving pathogenesis in the lung and have important implications for informing which therapy may be effective in SSA populations.

To address some of these knowledge gaps we conducted an autopsy study in well-characterised patients at a large public hospital in Malawi, a low-income country in SSA with high rates of malaria, TB and HIV. We undertook detailed histopathological analysis and scRNA-seq on lung, blood and nasal cells and imaging mass cytometry (IMC) to spatially resolve the immune landscape of the lung (Fig.1a). We conducted all tissue processing, cell dissociation and scRNA-seq library preparation on site in Malawi, with much of the data prepared on fresh samples. There are so far no studies from any settings that included characterisation across all these modalities. Thus, to fully understand the context of our data in contrast to other populations, we needed to use data from patient cohorts from different regions of the world to enable comparisons (Fig.1b). Taken together, our data highlight how Covid19 has a similar histopathological pattern in our SSA cohort to other Northern and Southern Hemisphere cohorts. However, we found a contrasting immune response signature in the SSA cohort, driven by proliferation of lung-resident alveolar macrophages and interferon gamma (IFN-γ).

Results

Clinical and histopathological analysis identifies a conserved histopathological signature of Covid19 in patients from SSA, in agreement with other Covid19 cohorts

We recruited patients with fatal illness aged 45-75 admitted to Queen Elizabeth Central Hospital, Blantyre (October 2020 and July 2021) and stratified into three groups based on clinical characteristics: 1) Covid19 acute respiratory distress syndrome (ARDS) (n=9), 2) lower respiratory tract disease (LRTD) (n=5) with ARDS of diverse non-Covid19 aetiology, 3) non-LRTD (n=2) (Fig.1b, Extended Data Table 1, see methods). Like other cohorts, fatal Covid19 cases were generally overweight or obese (78%) and several cases had type 2

133 diabetes (44%), whereas LRTD and non-LRTD cases were generally underweight. HIV was
134 common across all groups. No new diagnoses of HIV were made, and all infected cases had
135 been on highly active anti-retroviral treatment until stopping treatment during the
136 pandemic, reflecting challenges with access to healthcare and in keeping with low CD4
137 counts (median 134cells/mm^3).
138
139 Autopsies were conducted through minimally invasive tissue sampling (MITs)[19] using wide-
140 bore needle-biopsies. Lung, liver and brain samples were obtained in all 16 cases, bone
141 marrow in 15 cases and spleen in 8 cases. A pathologist (S.K.) read haematoxylin and eosin-
142 stained tissue slides alongside patients' history and antemortem lab results, per standard
143 clinical practice. In the lung in the Malawi Covid19 cohort the pathologist identified classical
144 features of Covid19 described in other cohorts[20-27], which were absent or less frequent in
145 LRTD cases (Supplemental Data Fig.1). In contrast, in other organs there were no Covid19
146 specific changes (Supplemental Data Table 1), focusing our further investigations on the
147 lung. Then, two additional pathologists (V.H., C.A.), blinded to diagnosis, scored the lung
148 pathology in all sixteen patients using more detailed semi-quantitative criteria developed by
149 us previously[13]. Within our Covid19 cases, type II pneumocyte hyperplasia, vascular
150 congestion, syncytia, granulation of tissue and lymphocyte infiltration were all significantly
151 more common and severe than in the non-Covid19 LRTD group; in contrast neutrophils
152 were more numerous in LRTD cases (Extended Data Fig.1a). There was no significant
153 difference in histopathology due to HIV status (Extended data Fig.1b).
154
155 Unfortunately, a lack of international consensus criteria for assessing Covid19 lung
156 pathology, and of studies with systematic scoring, prevented quantitative comparison with
157 other cohorts to assess similarities and differences. Therefore, we compared proportions of
158 different pulmonary lesion types with a study that combined cohorts from Europe and the
159 USA[21], and with our published Brazilian cohort[13] (Fig.1c). Acute alveolar changes, defined by
160 neutrophil infiltration and fibrin-deposition were more frequent in the Malawi and Brazil
161 cohorts than the USA cohort. “Chronic” alveolar changes with monocytes, macrophages or
162 fibrosis were detected more frequently in the USA and Malawi cohort. In the Malawi cohort,
163 “chronic” disease was predominantly characterized by macrophage and monocytes and
164 there was less fibrosis than in the USA and Brazil cohorts. The detection of macrophages by
165 histology in a high proportion of Malawi cases, despite a very short duration of illness, fits
166 with studies that observed inflammatory monocyte/macrophage populations in fatal
167 Covid19 cases with a short durations of illness[8,28,29], indicating a departure from classical
168 “acute” to “chronic” changes. Thus, despite a short duration from illness to death, and
169 demographic differences, cases in our Malawi cohort exhibited classical Covid19 lung
170 pathology.
171
172 **High-plex imaging highlights that Covid19 immunopathology is associated with alveolar**
173 **macrophages whereas LRTD is associated with neutrophils.**

174
175 To give cellular context to the histopathological features we made tissue microarrays,
176 identifying 130 representative regions of interest containing specific pathological lesions or
177 normal lung areas (9 Covid, 3 LRTD, 2 Non-LRTD cases). Tissue samples were analysed by
178 IMC using a 39 metal-conjugated antibody panel (Supplemental information) that we
179 previously optimised for staining in a Brazil cohort[13], an anti-SARS-CoV2 Spike (SARS-CoV2-S)
180 antibody validated in lung tissue[13,30]. After cell-segmentation and quality control, we
181 annotated 76,369 cells. Cells were divided into major subtypes and then subtypes classified
182 based on markers of activation, differentiation, proliferation and apoptosis (Fig.2a,
183 Extended data Fig.2a).
184
185 In our Malawi cohort, neutrophils ($CD66b^{pos}CD11b^{pos}CD14^{neg/low}$) were significantly more
186 numerous in the LRTD cases (49.6%) than in the non-LRTD (21.1%) or Covid19 cases (16.1%,
187 adjusted p=<0.001) (Fig.2b,d, Extended Data Table2 and Fig.2e). Reciprocally, macrophages
188 were increased in Covid19 (44.1%) compared to LRTD (30.4%) and non-LRTD cases (23.6%;
189 adjusted p=<0.0001, Fig.2b,c, Extended Data Table 2). In contrast to data in prior published
190 USA and European cohorts[28,30], these were predominantly alveolar macrophages
191 ($CD206^{high}CD163^{high}Iba1^{low}MHCII^{low}CD14^{neg}$) with a lower number of monocyte derived
192 $CD14^{high/int}$ cells.
193
194 There were no consistent differences in T-cell numbers between the Covid19, LRTD and
195 non-LRTD disease groups, but among Covid19 cases there was an expansion in Tregs and
196 proliferating T-cells and a decrease in the ratio of effector memory ($CD45RO^{high}$) to naïve
197 ($CD45RO^{low}$) CD8 T-cells (Fig.2b, Extended data Table 2). B-cell numbers were not markedly
198 different in Covid19, although we had few B-cell markers (Fig.2b). Consistent with vascular
199 pathology visualised by histology (fibrin deposition and thrombosis), there was increased
200 endothelial cell activation in Covid19 compared with LRTD and non-LRTD cases (Fig.2b,
201 Extended data Table2). Alveolar macrophages were the most common SARS-CoV2-S+
202 immune cell, followed by Arg^{high} neutrophils and interstitial macrophages (Fig.2b, Extended
203 data Table 2). In the stromal compartment type 2 pneumocytes (AT2) and epithelial cells
204 were the most frequent SARS-CoV2-S+ cells. We found no SARS-CoV2-S+ endothelial cells or
205 fibroblasts. Surprisingly, total numbers of SARS-CoV2-S+ cells were lower in HIV+ cases
206 (Extended data Fig.3c and Table 2).
207
208 Exploiting the spatial resolution of IMC and regions of interest selected based on a
209 dominant pathological lesion, we characterised cellular compositions of lesion-types
210 (Extended data Fig.2f), then quantified lesion-type levels by group (Fig.2e). Type II
211 pneumocyte hyperplasia was specific to the Covid19 group. Diffuse alveolar damage
212 occurred in both LRTD and Covid19 but had different compositions indicating different
213 pathological processes. In LRTD, diffuse alveolar damage was mainly associated with
214 neutrophil-driven fibrinopurulent inflammation; in Covid19, it had a more heterogenous

215 immune-cell composition, dominated by the presence of macrophages, except fibrin-
216 containing lesions which were neutrophilic. Together these implicate macrophages in
217 alveolar damage and lung parenchymal processes and neutrophils in coagulopathic
218 processes.
219
220 **Integration of high-plex data across Covid19 cohorts highlights shared different myeloid**
221 **compositions and low levels of cells containing SARS-CoV2 antigen in Malawi cases**
222
223 To systematically compare how the cell composition, degree of inflammation and amount of
224 virus differed between our Malawi cohort and other cohorts we integrated data from
225 Covid19 cases in our cohort (n=9) with two other cohorts that used IMC (Fig.2f): our Brazil
226 cohort (n=11) that employed the same antibody panel[22] and a USA cohort[30] (n=10) that
227 used several of the same markers including the same SARS-CoV2-S antibody. There were
228 many similarities in cell proportions between the three cohorts but also significant
229 differences (Fig2g,h). In the myeloid compartment there was a predominance of tissue-
230 resident myeloid cells in the Malawi cohort versus infiltrating cells in the USA cohort, the
231 Brazil cohort showed an intermediate phenotype. The USA cohort had the highest
232 proportion of neutrophils (26.28%; adjusted $p=2.64x10^{-12}$), and Malawi cohort the fewest
233 (7.9%, Brazil 19%). Monocyte/macrophages were more frequent in the Brazil (58.5%) and
234 Malawi (55.1%) than USA cohort (35.1%). Notably, the Malawi cohort had a high proportion
235 of apoptotic alveolar macrophages (12.9%) which were absent in the other two cohorts,
236 indicating that there may be specific macrophage responses in the Malawi cohort.
237 Endothelial activation was prominent in the Brazil and Malawi cohorts, and virtually absent
238 in the USA cohort (Fig.2h). In the stromal compartments there was a lower proportion of
239 fibroblasts in the Malawi cohort, in keeping with lower levels of fibrosis on histology.
240
241 SARS-CoV-2-S antigen gives an indication of the quantity of viral material, although does not
242 distinguish cells with replicating virus. We hypothesised that a tolerance-skewed immune
243 response might lead to higher levels of virus in Malawi cases but did not find evidence of
244 this. The USA cohort had the highest number of SARS-CoV2+ immune cells (25.7%, Malawi
245 13.9, Brazil 5%), These were principally monocytes and neutrophils in the USA cohort versus
246 alveolar and interstitial macrophages in the Brazil and Malawi cohorts (Fig.2g, Extended
247 Data Table 4). In the stromal compartment SARS-CoV2-S was detected in epithelial cells in
248 all three cohorts but were significantly lower in the Malawi (Fig.2h)(6.3%, $p=1.18x10^{-10}$)
249 compared to Brazil (13.1%) and USA (12.1%) cohorts.
250
251 We found no evidence of blunted immune response or higher viral loads in the Malawi
252 versus Brazil and USA cohort. The immune response signatures identified resident
253 macrophages in the Malawi cohort versus neutrophil and monocyte infiltration in the USA
254 cohort. A distinct apoptotic alveolar macrophage population in the Malawi cohort, together
255 with the prominence of alveolar macrophages in lung lesions (Fig.2e), led us to consider
256 whether these cells have differences in their inflammatory response in the Malawi cohort.

Pulmonary cell scRNA-seq reveals low levels of viral RNA and an IFN-γ dominated response in the Malawi cohort

To explore cellular responses in the lung at greater depth in our Malawi cohort, including in alveolar macrophages, we utilized scRNA-seq and single nuclei-sequencing (snRNA-seq) from 4 Covid19 cases, 3 LRTD cases and 1 non-LRTD case. Integrating 78,000 cells resulted in 16 cell clusters composed of a mixture of immune and stromal cells (Fig.3a).

SARS-CoV2 transcripts have been detected in scRNA-seq data in other postmortem cohorts[7,8]. We detected few SARS-CoV2 reads suggesting that at time of death there was minimal replicating virus (Extended data Fig.3). This is contrary to our initial prediction of tolerance and viral escape predominating in SSA populations but is consistent with our other data supporting inflammatory rather than direct viral-driven pathogenetic mechanisms.

We then undertook finer annotation of immune (Fig.3b) and stromal/vascular cell pools (Fig3c). We identified alveolar and interstitial macrophages and monocyte-derived-macrophages, consistent with monocyte/macrophage populations identified by IMC (Fig.2a,d). Both mature and immature neutrophils were present. Stromal cells included adventitial and alveolar fibroblasts as well as type I and II pneumocytes (AT1, AT2) and basal, secretory and ciliated epithelial cells. Cell proportions should be interpreted with caution given few cases per group, but they showed cell diversity expansion in the Covid19 and LRTD groups not observed or absent in the LRTD group (Extended data Fig.4a,b).

Principal differences in Covid19 compared to LRTD were in myeloid cells, particularly alveolar macrophages (Fig.3d,e), while few genes were expressed at higher levels in lymphocytes, dendritic cells or stromal cells (Extended data Table 3). In alveolar macrophages top differentially regulated genes included markers of tissue residency (C1QC, C1QB)[31] and factors shown to mediate lung fibrosis (CCL18)[32] and apoptosis (S1006)[33] and activation and recruitment of other myeloid cells (SPP1[34]. IFN-γ response protein (IFI30) and MHC proteins (HLA-DRA, HLA-DRB1) were all upregulated, indicating response to IFN-γ. SPP1 in alveolar macrophages is also linked with smoke-induced lung damage through IFN-γ induction[35].

This IFN-γ dominant response contrasts with Type I and III dominant interferon responses shown to be critical in pathogenesis in Northern hemisphere Covid19 cohorts[14,36]. Given our IMC data indicating a prominence of alveolar macrophages in the immune response and in alveolar damage we analysed alveolar macrophage interferon response modules: IFN-γ response pathways were strongly upregulated in Covid19 compared to LRTD. IFN-β, IFN-λ and TNF responses were also upregulated but to a lesser degree. Across other myeloid cell IFN responses were heterogenous and TNF response was upregulated in the LRTD group in CD4 T-cells (Extended Data Fig.4c).

303 **Integration with Human Lung Cell Atlas (HLCA): IFN-γ driven responses in Malawi cohort**
304 **and type I/III interferon responses in other cohorts**
305
306 To validate the IFN-γ response in the Malawi cohort compared to type I and III interferon
307 and IL1-dominant responses described in Northern hemisphere cohorts, and to understand
308 the implications for distinct therapeutic approaches we integrated our single cell data with
309 multi-cohort Covid19 (5 cohorts, 60 cases), LRTD (1 cohort, 13 cases) and non-LRTD (23
310 cohorts, 178 cases) data from the human lung cell atlas[10] (HLCA)(Fig.4a)(cohorts
311 summarised Fig.1b).
312
313 We used pathway analysis to profile cellular response differences between our cohort and
314 cohorts in the HLCA (Fig.4b). Pathways indicative of IFN-γ response were increased across all
315 cell types in the Malawi cohort (Fig.4b orange arrow). Furthermore, IFNG (IFN-γ gene) was
316 specifically increased in the Malawi cohort in CD4 and CD8 T-cells versus HLCA Covid19 and
317 Non-LRTD groups (Extended data Fig.5), suggesting that macrophages are responding to
318 IFN-γ produced by T-cells. Other inflammatory pathways showed a mixture of up and
319 downregulation in the Malawi cohort compared to HLCA cohorts, including IL6/JAK/STAT
320 (Fig.4b, green arrow) and TNF-NFKB (Fig.4b, blue arrow), key targets for therapies being
321 used in Covid19. Many of the other interferon-response genes were more upregulated in
322 the HLCA cohorts or had a heterogenous distribution across cells (Extended data Fig.5)
323 although notably monocyte-derived macrophages generally had a higher interferon
324 response in HLCA Covid19 cohorts (Extended data Fig.5).
325
326 These data show many shared inflammatory pathways between Malawi and HLCA cohorts
327 but with an amplified IFN-γ response in the Malawi cohort, highlighting IFN-γ production
328 from CD4/CD8 T-cells and response in alveolar macrophages.
329
330
331 **Single-cell analysis of nasal cells may be a useful proxy for lung parenchymal responses**
332
333 While lung is the principal organ involved in severe and fatal Covid19 disease, lung samples
334 are not easily accessible during life. For future Covid19 waves or other emerging diseases it
335 would be invaluable to predict lung responses using nasal or blood samples that can readily
336 be obtained.
337
338 We performed scRNA-seq on nasal cells in 8 cases (5 Covid; 2 LRTD and 1 non-LRTD) and
339 peripheral blood mononuclear cells in 7 individuals (4 Covid19, 2 LRTD and 1 non-LRTD). We
340 recovered 8,098 nasal cells which mapped to ten clusters composing immune and stromal
341 cells and 13,350 blood cells (Fig.5a,b). Nasal macrophages had several similar differentially
342 expressed genes in the Covid19 versus LRTD cases that mirrored lung alveolar macrophage
343 responses including SPP1 and C1QB, genes indicative of proliferation (LGALS1, TMSB10) and
344 MHCII genes (HLA-DPB1, HLA-DQA1) (Fig.5c). HLA-D upregulation is a canonical response to

345 IFN-γ[37] and consistent with this there was IFNG (IFN-γ gene) upregulation in T-cells in the
346 Covid19 cases in comparison to LRTD cases (Fig.5d). Pathway analysis showed higher levels
347 of IFN-γ response in macrophages and T-cells, further validating an IFN-γ response in these
348 cells (Fig.5e). Blood monocytes in Covid19 versus LRTD cases had upregulation of the
349 alarmin S100A12 and of genes involved in inflammation (AREG) and vascular damage
350 (NDRG1) but not in genes indicative of IFN-γ response and IFNG was not upregulated in T-
351 cells (Fig.5f). Hence in our small cohort nasal cells better paralleled lung response than
352 blood cells, supporting previous Covid19[38,39] and non-Covid19[40] studies that highlighted the
353 utility of nasal cells for understanding respiratory immune responses.
354
355 Since scRNA-seq is not available in most setting we assessed the extent to which cytokine
356 responses (Luminex) in plasma or nasal fluid could distinguish the inflammatory or IFN-
357 γ response in Covid19 versus LRTD cases. In nasal fluid there was a trend towards several
358 cytokines being higher in Covid19 cases than in LRTD cases, but none significant and no clear
359 difference for IFN-γ (Extended data Fig.6a). There was no clear blood circulating cytokine
360 response pattern, and no circulating cytokine levels were significantly higher in Covid19
361 compared to other groups (Extended data Fig.6b). A pseudobulk sequencing approach in
362 blood, nasal and lung cells also did not distinguish a clear IFN-γ or any other specific
363 inflammatory cytokine signature between Covid19 and LRTD cases (Extended data Fig.6c-
364 e). Single-cell methods identified an interferon signature and T-cell-macrophage axis, bulk
365 cytokine and gene expression approaches did not. Given very small numbers per group this
366 is perhaps unsurprising. It may stem from greater discriminatory power of single-cell
367 methods and is supportive of the value of single-cell approaches, particularly in small
368 cohorts.
369
370
371 **Stromal cellular interactions are driven by macrophages and vascular interactions by**
372 **neutrophils**
373
374 To validate our findings of the role of IFN-γ responding alveolar macrophages in lung
375 parenchymal pathology and neutrophil interactions in vascular pathology, and to predict
376 novel molecular interactions to target therapeutically we used cell interaction methods.
377 First, unbiased receptor-ligand analysis of our scRNA-seq data highlighted that a large
378 proportion of the imputed interactions in the lung involved alveolar macrophages,
379 interacting with fibroblasts, epithelial cells and other immune cells including CD4 T-cells
380 (Fig.6a), in keeping with our findings from cell proportions, cellular histology and scRNA-seq.
381
382 To validate these interactions in a spatial context we used neighbourhood enrichment
383 analysis of IMC data to identify cells located close to each other with greater than expected
384 frequency as an indicator of their likelihood to be interacting (Fig.6b,c). In the non-LRTD
385 there were no significant interactions (Extended Data Fig.7). The LRTD group was

386 completely dominated by neutrophil interactions (Fig.6b). In the Covid19 group several
387 neighbourhood enrichments were prominent – principally alveolar macrophages (with and
388 without SARS-CoV2-S and apoptosis) with apoptotic fibroblasts and to a lesser extent type II
389 pneumocytes (Fig.6c). This supports the role in pathogenesis of alveolar macrophages
390 including the apoptotic population present in Malawi but not USA or Brazil cohorts. In
391 contrast the most prominent neighbourhood enrichment for neutrophils was between
392 SARS-CoV2-S+,Arg^{high} neutrophils and activated endothelial cells implicating neutrophils in
393 endothelial/vascular pathology.
394
395 We then looked at validated interactions in Covid19 in closer detail in scRNA-seq data.
396 Macrophage interactions were frequently from ligands on type II pneumocytes to receptors
397 on alveolar macrophages (Fig.6d), in keeping with type II pneumocytes cells generally being
398 a principle infected cell[41]. Several of these interactions involved macrophage inhibitory
399 factor (MIF) from type II pneumocytes with CD74, CD44 and CXCR4 on macrophages, a
400 classical response chain in macrophages and a key initiator of proliferation, chemotaxis and
401 activation[42]. ICAM-1 on type II pneumocytes was predicted to signal to integrins (ITGB2-
402 ITGAM) on alveolar macrophages, an interaction involved in cellular attachment during
403 recruitment. Another strong predicted interaction was IL-34-CSF1R, involved in triggering
404 macrophage activation and chemotaxis. Reciprocally there were several interactions
405 between alveolar macrophages and epithelial cells consistent with our IMC data that
406 indicate their role in alveolar pathology. These included SPP1 and TGFβ with type II
407 pneumonocyte integrins (ITGB6) (Fig.6e), interactions implicated in lung pathology and
408 fibrosis[34,35,43]. We identified multiple neutrophil interactions with endothelial cells indicating
409 processes involved in neutrophils attachment to the vascular wall (e.g., ITGAL-ICAM-1) and
410 of activation by neutrophil granule proteins (GRN-TNFRSF1A) (Fig.6f,g), providing molecular
411 validation supporting their role in coagulation, endothelial activation and vascular pathology
412 indicated by IMC.
413
414 These data highlight the value of a combined scRNA-seq and IMC approach. They provide
415 spatial and receptor-ligand validation for roles of alveolar macrophages in molecular
416 processes that are plausibly involved in alveolar damage and lung fibrosis, and for
417 neutrophils in endothelial activation. The data predict specific molecular interactions
418 involved in these processes. If validated by further work, some of these interactions may be
419 plausible targets for intervention, e.g., MIF for which several small molecules are in clinical
420 development for therapy in inflammatory disorders[42].
421
422
423 **Discussion**
424
425 We conducted minimally invasive autopsies on fatal Covid19 and other LRTD and non-LRTD
426 cases in a Malawian population and characterised pulmonary, blood and nasal immune

427 responses using scRNA-seq and IMC. While other studies have used these techniques for
428 Covid19 investigations in other settings, this is the first such study in a SSA population and
429 to our knowledge some of the first scRNA-seq data from lung samples in any SSA
430 population. Our de-identified data are provided open access, including tools for visualising
431 single-cell and histology data, making an important resource for furthering the global
432 understanding of Covid19 pathogenesis, immune responses in SSA populations and more
433 widely for the human cell atlas.
434
435 Given that many parasitic infections induce immune tolerance we hypothesised that there
436 might be an attenuated immune response in SSA populations, blunting immune-mediated
437 viral clearance and leading to high viral-loads in individuals who present with life-
438 threatening disease. If so, pathology might be driven by direct-viral effects rather than
439 hyperinflammation, indicating a need for different treatment approaches from Northern
440 hemisphere cohorts. In fact, we found a robust immune response and comparatively low
441 levels of virus, surprisingly even in highly immunosuppressed cases with HIV. Our data
442 indicate that pathology is driven by inflammation, with many similarities to other non-
443 African cohorts, in both histopathology and immunology. These similarities are reassuring,
444 indicating that many principles for diagnosis and treatment can likely be extrapolated from
445 more extensively investigated populations. However, there were also differences that may
446 have implications for therapy, in particular IFN-γ responses were upregulated in comparison
447 to a large multi-country integrated HLCA dataset. IFN-γ was produced by T-cells, with
448 alveolar macrophages the principle responding cells. Using IMC, we showed that these
449 resident macrophages were the dominant cell in pathological lesions. Spatially-resolved IMC
450 interaction analysis and scRNA-seq receptor-ligand analysis orthogonally validated these
451 processes. In contrast IL6 and TNF responses were not as prominent. scRNA-seq of nasal
452 cells also identified IFNG upregulation in T-cells and evidence of IFN-γ response in
453 macrophages in a sample type that is readily accessible, supporting prior data on the utility
454 of nasal cells as an accessible proxy for lung responses.
455
456 There is cross-over between the responses of different interferons and IFN-γ signal has been
457 detected previously in Covid19 lung[7], yet it is interesting to consider why there was such a
458 marked upregulation in our cohort compared to the large integrated HCLA dataset. IFN-γ
459 response has been shown to be a key component of effective immunity to malaria and is
460 augmented in malaria exposed individuals, in part through epigenetic changes termed
461 trained immunity[17]. Increased IFN-γ response was a key difference in SSA (Gabon) versus
462 European individuals exposed to controlled human malaria infection and a correlate of
463 protection[16]. While type I/III interferons are more typically involved in clearance of SARS-
464 CoV2 and other respiratory viruses[44], IFN-γ also plays a role, particularly in macrophages[45].
465 Considering our data with these prior studies we propose that trained immune responses to
466 prior infections may favour an accelerated macrophage IFN-γ response. We hypothesise
467 that this may be a double-edged sword in Covid19 in SSA: such an accelerated trained

468 response may generally be protective (through more rapid viral clearance), but in a subset
469 of patients it may lead to accelerated hyperinflammation and collateral tissue damage. This
470 hypothesis is supported by the short time between symptom onset and death in our cohort
471 already with a clear hyperinflammatory response. Further exploration of macrophage
472 responses in both SSA and non-SSA populations is therefore warranted.
473
474 Considering the potential for translation the existing therapies for Covid19 target JAK/STAT
475 (Barcitimib), IL6 (Toculimazab/sarilumab) or TNF (infliximab)[14,15]. JAK/STAT signalling is a
476 conserved pathway for interferon responses including IFN-γ[45]. Thus our data, if
477 corroborated, support potential efficacy of Baricitinib over other treatments. Barcitinib is a
478 small molecule (tablet) and thus highly suited to wide distribution[15].
479
480 Our data have several limitations. Our cohort was small and in a single centre. Although
481 single-cell methods have a higher capacity to resolve complex data in small sample sizes,
482 many analyses in our study were underpowered. It is thus unclear how representative our
483 data are of the wider Malawi or other SSA populations. Studies in other settings and ideally
484 large multi-centre studies, are needed. While this would be a complex undertaking, we have
485 demonstrated that single-cell methods are feasible in a SSA setting, and our study provides
486 useful templates. While lung samples cannot readily be obtained in live patients,
487 postmortem studies have limitations: cells may change or degrade; pathological processes
488 present early in disease are likely missed. Yet, postmortem studies in northern hemisphere
489 settings with longer postmortem intervals identified validated targets[7]. While minimally
490 invasive autopsy is more feasible and acceptable than traditional open autopsy, blind
491 sampling may attenuate the identification and sampling of areas of pathology. However,
492 except for large airway pathology, which was not sampled, most Covid19 features were
493 identified. The studies that we used for comparisons had significant variation in methods
494 and demographics from ours which may induce noise and bias. We used data-integration
495 methods which reduce but do not eliminate this. Reassuringly findings were validated both
496 by comparison to Human Lung Cell Atlas and orthogonal IMC data.
497
498 Our data establish the feasibility and utility of single-cell analyses in postmortem studies in a
499 SSA setting and provide a resource of lung, blood and nasal cells alongside histology and
500 spatial characterisation on a population not yet represented in the human cell atlas. Our
501 work indicates differences in the Covid19 inflammatory response among a Malawian cohort
502 compared to other non-African cohorts, highlighting IFN-γ as a potential target for
503 intervention and supporting the utility of scRNA-seq of nasal samples to assess respiratory-
504 tract immunology in LRTD.
505
506
507
508

Online Methods

Ethics and sensitisation

The study protocol was approved by the National Health Scientific Research Committee (NHSRC) in Malawi (Protocol number 07/09/1913) and by the Medical Veterinary Life Sciences ethics committee in Glasgow (protocol number 200190041). Informed consent was taken from the families of deceased patients. We underwent a full sensitisation process for the study with all staff on the recruiting wards in our hospital to discuss the study and consider the best way of sensitively conducting recruitment and informed consent. This work was led by two social scientists (L.S., D.N.) one with specialised in Bioethics (D.N.). Details of our approach and considerations for recruitment are published separately (*In press*).

Patients

We recruited patients aged 45-75 admitted to Queen Elizabeth Central Hospital, Blantyre between October 2020 and July 2021 during which there were two epidemiological waves driven by different SARS-CoV2 variants: Beta (Dec 2020-Feb 2021) and Delta (May-July 2021). Patients admitted with respiratory signs were routinely tested for SARS-CoV2 at QECH. We recruited cases into three groups based on clinical criteria: 1) a Covid19 group (n=9) with clinical features suggesting acute respiratory distress (ARDS, oxygen requirement and either respiratory signs on clinical examination or chest x-ray changes or both) and who had at least one nasal swab positive for SARS-CoV2 on admission; 2) A non-Covid19 LRTD (lower respiratory tract disease) group (n=5) who had clinical signs of ARDS but were negative for SARS-CoV-2 on admission and during hospitalization; 3) a no LRTD, COVID-19 negative group (n=2) who had no oxygen requirement and no clinical signs of LRTD and for whom the admission and any subsequent nasal swabs were negative for SARS-CoV2 on PCR (Fig.1b, Extended Data Table 1). The study only recruited cases who died between 12 midnight and 12 noon to minimise the postmortem interval and to avoid doing any autopsies at night.

Minimally invasive autopsy

We used minimally invasive sampling to conduct autopsies with large-bore needle biopsies of organ samples rather than full autopsy[19]. Being more culturally acceptable, MITS is widely used to determine cause of death in paediatric studies[19,46-48], showing good concordance with full autopsy[46]. From our ongoing paediatric MITs studies in Malawi, we adapted protocols for adult patients with Covid19 to obtain tissue suitable for single cell RNA-sequencing (scRNA-sequencing) and IMC. Based on CHAMPS but with adaptations. In particular, a larger calibre needle (11 gauge) was used for biopsies to obtain larger tissue samples. Samples were taken from the brain from supraorbital sampling from both left and right sides. From each lung samples were taken from lower middle and upper zones from a

550 single entry-point, angling the needle to sample different areas. Nasal cells were collected
551 from the nasal inferior turbinate using curettes (ASL Rhino-Pro, Arlington Scientific). Two
552 curettes were collected from each nostril and the cells placed immediately into ice cold
553 Hypothermosol (StemCell). Cells were transported on ice in a cold box immediately to the
554 lab and were spun at 300g for 5mins either for immediate processing for scRNA-seq or were
555 stored in Cryostor 10 (see below). Nasal fluid was collected using matrix strips
556 (Nasosorption, Hunt Developments). One strip was used per nostril.
557
558 PPE was worn by all staff involved in the autopsies and for all work in the lab. Lab work on
559 samples was done in vented laminar flow hoods.
560
561 **Processing of Storage of samples**
562 Biopsies from each organ were collected in three different ways for different downstream
563 workflows: 1) for paraffin embedding for histology and IMC put in 10% neutral buffered
564 formalin, 2) for viable cells put in ice cold hypothermosol (StemCell) for transport to the lab
565 and then slow frozen in Cryostor 10 (StemCell), 3) for snap frozen cells put in cryovials which
566 were then sealed and immediately submerged in liquid nitrogen.
567
568 Biopsies were fixed in 10% neutrophil buffered formalin for 4 - 8 hours, rinsed in water and
569 then embedded in paraffin blocks. Samples for viable cells were rinsed and cut into pieces of
570 approximately 20mm – 50mm and then put into ice cold cryostor for 15 – 30 mins before
571 transfer to a -80°c freezer in a chilled cryogenic storage container (CoolCell, Corning).
572
573 Blood cells collected into sodium heparin tubes were separated from plasma by spinning at
574 400g for 10 minutes. Plasma was then removed and spun for an additional 10 minutes at
575 1500g and plasma frozen in aliquots at -80°c. Cells were resuspended in 10% fetal bovine
576 serum in PBS and PBMCs were separated using ficoll histopaque with a 27min spin at 450g
577 and either used immediately for scRNA-seq or pelleted and resuspended in ice cold Cryostor
578 10 and then moved to a -80°c freezer in a chilled cryogenic storage container (CoolCell,
579 Corning). The following day samples were moved from the -80°c freezer to liquid nitrogen
580 for long term storage. Snap frozen samples were transferred in a liquid nitrogen dewar and
581 then moved to liquid nitrogen storage tanks for long-term storage.
582
583
584 **Pathology and organ specific scoring**
585 Formalin-fixed tissues were paraffin embedded (FFPE) for lung, bone marrow, brain, spleen,
586 and liver to make blocks. FFPE blocks were sectioned at 2-4 μm thickness, mounted on glass
587 slides and stained with haematoxylin and eosin (H&E). A medical pathologist (S.K.) reviewed
588 tissue slides, alongside patients' history and antemortem lab results, per standard clinical
589 practice and also completed an organ specific scoring proforma that included Covid19
590 features (Supplemental table 1). Then, for a non-biased assessment, two additional

591 pathologists, blinded to diagnosis, scored the lung pathology in all patients using systematic
592 scoring criteria[49]. Lung tissue was scored independently by two additional pathologists (C.A.
593 and V.H.), who were blinded to patient history and previous diagnoses. Following individual
594 scoring, any discrepancies were agreed by joint review of the slides until a consensus was
595 reached. The lung scoring was semiquantitative for the parameters indicated in Extended
596 data, Fig.1a-c. Subsequently, we characterised each sample with a dominant histological
597 characteristic, e.g., fibrinopurulent inflammation/pneumonia in case the neutrophil
598 infiltration with fibrin-extravasation was marked next to a mild infiltrate of lymphocytes,
599 plasma cells and macrophages. Whole tissue slides from lung samples in our 9 Covid19 cases
600 can be accessed in their entirety, and visualised at various magnifications, as if they were
601 observed under a microscope using our virtual microscope tool: https://covid-
602 atlas.cvr.gla.ac.uk (de-identified slides will be uploaded and publicly viewable on
603 publication).
604
605 After scoring, in each lung biopsy, the most representative areas were manually selected
606 based on the scoring performed on the H&E-stained section to create the tissue microarrays
607 (TMA) with cores of 1mm in diameter using the TMA Grand Master (3Dhistech, USA) and
608 CaseViewer software (version 2.4.0119028). At least 8 regions of interest were taken from
609 each case (4 left, 4 right). From the newly created TMA-FFPE-blocks, 4 μm thick sections
610 were cut and used for downstream imaging mass cytometry (IMC).
611
612
613 **Cause of death attribution**
614 A panel consisting of the pathologist who reviewed the cases, respiratory physician,
615 intensive care physician, infectious disease physician and two trainee doctors reviewed all
616 the cases to assign a cause of death. Codes assigning death were given according to ICD
617 codes and using the standard coding system used for death certification. The review
618 consisted of a review of the clinical notes, pre and post mortem lab results and the
619 pathology report. Each member reviewed the documents independently and reached an
620 individual verdict. When there was discrepancies a consensus was reached through
621 discussion.
622
623 **Multiparameter Cytokine Assay**
624 Cytokine levels were measured in plasma and nasal fluid samples using Luminex with the
625 Inflammation 20-Plex Human ProcartaPlex™ Panel (Thermofisher, EPX200-12185-901)
626 according to the manufacturers protocol and levels measured with a Luminex MagPix
627 device. Data were transformed with a log2 and for the visualistion with ComplexHeatmap in
628 R with a Z-score by gene. For the statistical tests of genes associated with the IFN-γ pathway
629 we used a Welch Two Sample t-test. No significant differences for those genes was found
630 between the Covid-19 and LTRD samples.
631

632
633 **Imaging mass cytometry (IMC)**
634 Sections from tissue micro arrays underwent deparaffinisation, followed by antigen retrieval
635 at 96°C for 30 min in Tris-EDTA at pH 8.5. Non-specific binding was blocked with 3% bovine
636 serum albumin for 45 min, followed by incubation with lanthanide-conjugated primary
637 antibodies (overnight at 4°C) which were diluted in PBS with 0.5% BSA (Table of antibodies
638 in Supplemental information). Antibodies were conjugated with metals using Maxpar
639 Antibody Labeling Kits (Standard BioTools) and were validated with positive control tissue
640 (tonsil and spleen for immune-targeted antibodies). Slides were then washed with 0.1%
641 Triton-X100 in PBS, followed by nuclear staining with iridium (1:400, Intercalator-Ir,
642 Standard Bio Tools) for 30 minutes at RT, and finally briefly (10 s) washed with ultrapure
643 water and air-dried. Images were acquired on a Hyperion imaging mass cytometer as per
644 manufacturer's instructions (Standard BioTools). Each TMA core was imaged in a separate
645 region of interest.
646
647
648 **Imaging Mass Cytometry (IMC) analysis.**
649 Preprocessing, imaging denoise, cell segmentation and extraction of single-cell features
650 were performed using a combination of Python and R packages, such as
651 ImcSegmentationPipeline, IMC-Denoise[50] and DeepCell[30,51] as described previously[13].
652 Briefly, for the single-cell analysis, the annotated data object was generated, protein
653 expression raw measurements were normalized at the 99th percentile to remove outliers. In
654 Scanpy (Single-Cell Analysis in Python v 1.9.1)[52] PCA, batch-correction and harmony data
655 integration was performed to compute and plot the UMAP embeddings (umap-learn Python
656 package, v 0.5.3). Next, automated cell type assignment using the Python package Astir
657 (ASsignmenT of sIngle-cell pRoteomics v 0.1.4)[51], was applied to identify the major cell types
658 expected to be found in the lung tissue according to the antibody panel utilized. For cell
659 assignment with Astir, the following information to label cells based on a broad ontogeny
660 (metaclusters and major cell types) and the proteins (lineage markers) to be most expressed
661 in each expected cell type were used. Metaclusters and major cell types: (a) myeloid:
662 macrophage, neutrophil; (b) lymphoid: CD8 T cells, CD4 T cells, B cells; (c) vascular:
663 Endothelium, red blood cells (RBCs); (d) stromal: fibroblast, smooth muscle cell, epithelial.
664 Cell types: (a) macrophage: CD163, CD206, CD14, CD16, CD68, CD11c, Iba1; (b) neutrophil:
665 CD66b, Arginase1; (c) CD8 T cells: CD3, CD8; (d) CD4 T cells: CD3, CD4; (E) B cells: CD20; (f)
666 endothelium: CD31; (g) fibroblast: Collagen1; (h) smooth muscle cell (SMC): SMA; epithelial:
667 PanCK; RBCs: CD235ab.
668
669 After cell assignment, cells labelled as "other" or "unknown" were filtered out from
670 downstream analysis, the annotated data object was subset into the major cell types
671 identified, i.e., macrophages, neutrophils, lymphoid, vascular, epithelial and stromal and
672 Phenograph Louvain clustering (with 200 nearest neighbors)[53] was performed for each cell

673 population separately using a small set of specific lineage marker and functional proteins, as
674 previously described[13]. The finer cell type annotation was used to evaluate the frequency
675 and absolute counts of cell types across clinical groups, histopathological lesions and HIV
676 status. Differential abundance analysis was also performed using the scanpro and scCODA
677 Python's packages[54] and miloR R package (v 1.4.0)[55]. Spatial statistics analysis based on the
678 coordinates of the cells in the ROIs, were performed using the Python packages Squidpy
679 (Spatial Quantification of Molecular Data in Python v. 1.2.2)[56]. Building of the spatial graph,
680 calculatin and plotting of the neighborhood enrichment scores were performed as
681 previously described[13].
682
683
684 **Integration of Malawi IMC data with other available IMC COVID-19 lung data.**
685 IMC COVID-19 data from post-mortem lung samples from a Brazilian[13] and US[30] fatal cohort
686 were integrated with the Malawi IMC dataset. First, datasets were concatenated in Scanpy
687 taking the "inner" (intersection) of all common protein markers in the panels across the 3
688 IMC datasets. Then, with scvi-tools[57] we applied different integration methods, such as
689 harmony and variational autoencoder (VAE)-based methods, such as scVI and scANVI.
690 Analysis of the UMAP embedding of the integrated versus non-integrated data showed that
691 harmony and scANVI performed better and in downstream analysis we used harmony-
692 integrated output. Next, cell identities were standardized (label harmonization), which
693 refers to a process of checking that labels are consistent across the datasets that are being
694 integrated. Finally, cell frequencies in the post-mortem lung across all 3 cohorts were
695 plotted and differential abundance analysis was performed using scanpro
696 (https://github.com/loosolab/scanpro) and scCODA Python's packages[54] and miloR R
697 package (v 1.4.0)[55].
698
699
700 **Dissociation of lung cells from frozen samples and single nuclei preparation.**
701 Lung samples were dissociated both from fresh samples and from slow frozen samples that
702 had been stored in liquid nitrogen. Slow frozen cells were defrosted using a defrosting
703 protocol described previously[7]. Fresh or defrosted frozen cells were then dissociated
704 adapting methods developed previously[58]. Briefly cells were dissociated in a buffer
705 containing 400µg/mL of Liberase DL (Sigma), 32U/ml of DNAse I (Roche) and 1.5% BSA in
706 PBS (without calcium and magnesium). The tissue was put in buffer (4 times weight:volume)
707 in a GentleMACS C-tube *(Miltenyi 130-096-334)* minced with scissors and then run on a
708 GentleMACS dissociator (*130-093-235) on* programme "C-lung 01_02". Dissociation was
709 achieved by warming tissue on an orbital shaker in a chamber at 37C for 30 mins and
710 running "C-lung 01_02" twice more; once at 15 mins and once at 30mins. Enzyme was
711 neutralised by diluting with 10ml of ice cold 20% FBS with 32u/ml of DNase and the sample
712 was filtered through a 100µM strainer (352360) and samples were subsequently kept on ice
713 with all centrifuge and antibody incubation steps at 4c. Cells were pelleted by spinning at
714 300g for 5 mins and red cells removed by incubation with ACK buffer for 5mins. For frozen

715 cells debris were removed using a debris removal solution (Miltenyi, 130-109-398) according
716 to the manufacturers protocol. Single nuclei were prepared from snap frozen lung samples
717 as described previously[7]. Briefly, frozen lung tissue was kept on dry ice/ liquid nitrogen until
718 processing was started. Tissue was added to a gentle MACS C-tube containing 2ml of freshly
719 prepared nuclei extraction buffer which contained RNAse inhibitors; 0.2 U/µL RNaseIN Plus
720 RNAse inhibitor (Promega) and 0.1 U/µL SUPERasin RNAse inhibitor (Thermofisher
721 scientific). Dissociation was achieved by running the C-tube on GentleMACs dissociator on
722 program ''m_spleen_01'' for 1 minute. The sample was then filtered using a 40 µM strainer.
723 The C-tube and strainer were rinsed using a buffer containing 0.1% enzymatics RNAse
724 inhibitor (Enzymatics). Sample was then pelleted by spinning at 500g for 10 minutes at 4^0C.
725 Pellet was then resuspended in 500ul of 1xST without RNAse Inhibitor. The sample was then
726 filtered using 35µM strainer, a 10 µL volume was loaded on haemocytometer for counting.
727
728
729 **Single cell and single nuclei partitioning and library preparation**
730 10x 3' 3v chemistry was used for all samples. For fresh lung samples we loaded 10,000 cells
731 into one channel of a 10x chip (1000120). For fresh nasal and blood samples we labelled the
732 nasal and blood samples with different hashtags and pooled them at a 1:1 ratio and loaded
733 10,000 – 20,000 cells. For frozen nuclei and single cell samples we pooled samples from 3 –
734 6 different cases aiming for equal ratios and loaded 20,000 – 40,000 cells/nuclei. Libraries
735 were prepared according to the manufacturers protocol and sequenced with an Illumina
736 NextSeq2000. To make these data available for analysis by others, reads were submitted to
737 ArrayExpress (E-MTAB-13544).
738
739 **Analysis of single cell data**
740 The reads were mapped using Cellranger (version 7, including introns) to a combined
741 reference of human, Covid19. For mixed genotypes, samples were separated using
742 SoupOrCell[59], and for hashtag oligonucleotide labelled mixes of nasal and blood samples
743 from the same patient, the CiteSeq protocol was followed. Data analysis was conducted in R
744 version 4.2.1, utilizing Seurat[60] for data integration within each tissue and with the Human
745 Lung Cell Atlas (HLCA) using Harmony. Differential expression analysis was performed with
746 MAST, and cell-cell interactions were assessed using multinichenetR
747 (https://www.biorxiv.org/content/10.1101/2023.06.13.544751v1). All figures were
748 generated in R. The different datasets are accessible on the Glasgow Cell Atlas website:
749 http://cellatlas.mvls.gla.ac.uk/. See additional details in supplemental information.
750
751
752 **Funding and Acknowledgements**
753 We would like to thank families who agreed to take part in this research and all health care
754 professionals at Queen Elizabeth University Hospital who cared for the patients during life,
755 supported bereaved families and helped with recruiting patients and morticians who helped
756 with autopsies. We thank Brigitte Dennis and staff at the Core laboratory at Malawi

Liverpool Wellcome for help with processing laboratory samples, Dr Gareth Howell and the University of Manchester Flow Cytometry Core Facility for helping with the IMC investigations and David McGuinness and Julie Gilbraith and other staff at Glasgow Polyomics for technical advice and help with sequencing of single-cell and single nuclei libraries, Monica Soko and Karl Seydel at Blantyre Malaria Project laboratory at KUHES for running the Luminex samples. We would like to thank Alex Shalek, Sergio Heli Triana Sierra and Chloe Villani for technical advice and Alex Shalek for shipping reagents to Malawi when we could not obtain them from our suppliers. We thank Megan McLeod for suggestions on the manuscript. This work was funded through a grant to C.A.M. from the Bill and Melinda Gates Foundation (INV-018138). C.A.M. is a UKRI Medical Research Council (MRC) MRC Future Leaders Fellow (MR/V025856/1). K.N.C. was supported by the MRC (MR/R010099/1). MR/R010099/1 was jointly funded by MRC and the UK Department for International Development (DFID) under the MRC/DFID Concordat agreement and was also part of the EDCTP2 program supported by the European Union. M.M. is supported by a Wellcome Center award (number 104111). J.LS.F. was supported by the Sao Paulo Research Foundation (FAPESP grant 2019/015782 and 2016/12855-9) and it is currently supported by MRC (MR/W018802/1). F.T.M.C is supported by the Sao Paulo Research Foundation (FAPESP grants 2020/05369-6 and 2017/18611-7). W.M.M. is supported by the Amazonas Research Foundation (FAPEAM N. 005/2020 - PCTIEMERGESAÚDE – AM). M.V.G.L., G.C.M., W.M.M. and F.T.M.C. are CNPq research fellows. The University of Glasgow Wellcome Centre for Integrative pathology (104111) and Malawi-Liverpool-Wellcome Programme are supported by Core funding from Wellcome. This publication is part of the Human Cell Atlas — www.humancellatlas.org/publications/

Data Availability Statement

scRNA-Seq: Raw data and processed count matrices are deposited at the EBI ArrayExpress (Accession number E-MTAB-13544 (private until publication). Fully processed .RDS objects of the scRNA-seq analysis and IMC can be found through the GitHub repository (see Code Availabilty Statement). The atlases are browsable using the cellxgeneVIP platform hosted by the University of Glasgow at the following URLs:

Lung Atlas - https://cellatlas-cxg.mvls.gla.ac.uk/COSMIC/view/COSMIC_Lung_Atlas.h5ad/

Lung Immune Atlas - https://cellatlas-cxg.mvls.gla.ac.uk/COSMIC/view/COSMIC_Lung_Immune_Atlas.h5ad/

Lung Stromal Atlas - https://cellatlas-cxg.mvls.gla.ac.uk/COSMIC/view/COSMIC_Lung_Stromal_Atlas.h5ad/

Nasal Atlas - https://cellatlas-cxg.mvls.gla.ac.uk/COSMIC/view/COSMIC_Nasal_Atlas.h5ad/

Blood Atlas - https://cellatlas-cxg.mvls.gla.ac.uk/COSMIC/view/COSMIC_Blood_Atlas.h5ad/

Histopathology slides on virtual microscope: https://covid-atlas.cvr.gla.ac.uk

Metadata for the cases (without identifying information) is provided in Extended Table 1.

IMC - https://cellatlas-cxg.mvls.gla.ac.uk/COSMIC/view/COSMIC_IMC_Lung.h5ad/

Code Availability Statement

801 All R scripts for the scRNA-Seq analysis and figure generation can found at
802 (https://github.com/olympiahardy/COSMIC_Malawi_Covid_Atlas). Python scripts to process
803 the imaging mass cytometry and figure generation can also be found at the above
804 repository.
805
806
807 **Author contributions**
808 Research protocol, Malawi (CAM, VW, DN); Sensitisation, Malawi (LS, TN, MS, DN);
809 Recruitment of patients, Malawi (MS, TN, LS, DN, DC, CE, AT, FZ) ; Autopsies, Malawi (SK,
810 CA); Pathology report, Malawi (SK); Histopathology scoring and identification of regions of
811 interest (CA, VH); Clinical characterisation and cause of death attribution, Malawi (TN, MS,
812 SK, PB, BM, SL, VW, DD), Lab protocols and processing of tissues, Malawi (JN, CN, FD, WN,
813 TN, SK, CP, CAM), Set up of single cell protocols and optimisation of single cell methods,
814 Malawi (JN, CAM), Single cell experiments (JN, CAM, CN, LN, JP); designed and conducted
815 IMC experiments (MH, KC); Analysis of histology data (CA, VH, CAM) Analysis of single cell
816 data (OH, TO); Protocols, sample collection and processing of Brazil samples (M.F., F.F.AV.,
817 M.B., C.C.J.,T.T. and V.S.S); Analysis of IMC data (J.L.); Prepared figures (OH, JL, TO, KB,
818 CAM); Uploaded data onto repositories and interactive modules (OH, TO, VH);
819 Conceptualisation (CAM, TO, VW, DD, SK); Wrote the grant (CAM, TO, DD, VW, BK);
820 Supervision (CAM, TO, MM, DD, VW, KC, SK, MP); Drafted the manuscript (C.A.M.); Edits of
821 the manuscript (JN, OH, JL, KB, KC, MP, DD, MM, TO), all authors reviewed and approved the
822 final manuscript.
823
824
825
826 **Figure Legends – Main Figures**
827
828 **Figure 1** | *Study overview, overview of our cohort and comparator cohorts and histological*
829 *lesion comparison with other cohorts*.
830 **A)** Overview of study approach, image created using BioRender; **B)** Summary of the
831 characteristics of our Malawi cohort versus published cohorts that we have used for
832 different comparisons. **C)** Heatmap shows the proportion of cases in the three cohorts
833 (USA/European; Malawi; Brazil) that have each given lesion type.
834 Abbreviations:
835 SS to death = symptom start to death in days.
836 Path = Pathology. indicates the number of cases included in each cohort in which
837 postmortem pathological features are described.
838 Sys. Hist. = Systematic histopathology, denotes the number of cases included in each cohort
839 with scoring of the frequency and severity of different lesions scored based on pre-defined
840 criteria.
841 IMC = Imaging Mass Cytometry, number of cases with data for this.
842 Lung sc = lung cell single-cell RNA-seq, denotes the number of cases with scRNA-seq data
843 from lung tissue.
844 nasal sc = Nasal cell single-cell RNA-seq, denotes the number of cases with scRNA-seq data
845 from nasal tissue.
846 blood sc = blood cell single-cell RNA-seq, number of cases with this data
847

848 **Figure 2 |** *Imaging Mass Cytometry (IMC) reveals an immunopathological landscape of*
849 *Covid19 in Malawi cases driven by alveolar macrophages*
850 **A)** UMAP embedding of the cell types identified in the lung samples by IMC, after supervised
851 assignment to major cell types. Each major cell type was clustered and resulting clusters
852 were annotated and merged to extract the final set of cell types. Colour key for cell types is
853 on right hand side of B. **B)** Frequency of the immune cell types identified in the post-
854 mortem lung samples by IMC according to clinical groups. The stacked bar plot shows the
855 averaged frequency of the cell types by grouping the values from regions of interest (ROIs)
856 according to the clinical groups. Dashed lines highlight principle differences in major cell
857 populations between COVID-19 and other respiratory disease groups. **C)** Representative
858 denoised IMC images from COVID19 case shows high levels of $CD206^+$ macrophages (yellow)
859 and lower levels of neutrophils (CD66b, red) and monocytes (CD14, purple). **D)**
860 Representative denoised IMC images from LRTD case shows high levels of high levels of
861 neutrophils (CD66b, red) and low levels of $CD206^+$ macrophages (yellow). **E)** Frequency of
862 histopathological lesions based on matched H&E and IMC analysis of post-mortem lung
863 samples from the different clinical groups. The cellular composition and frequency of
864 different cell types is indicated in Extended data Fig. 3F. **F)** UMAP embedding of the
865 integrated IMC lung data from the Brazil, USA and Malawi COVID-19 cohorts. **G)** Comparison
866 of immune cell frequencies in IMC data from Brazil, Malawi and USA cohorts after
867 integration shown in F, some major cell group differences are highlighted by dotted lines.
868 Dashed box highlights apopototic alveolar macrophages which are only present in the
869 Malawi cohort. **H)** Comparison of stromal cell frequencies in IMC data from Brazil, Malawi
870 and USA cohorts after integration shown in F.
871
872 **Figure 3** | *Lung single cell atlas highlights IFN-γ response in alveolar macrophages*
873 **A)** UMAP visualisation of 66,882 lung cells across our cohort, coloured by broad cell types.
874 Outer circos tracks denote the proportion of each cell type across our three disease groups
875 (COVID-19 orange, LRTD blue and No-LRTD green) and whether the cells belong to patients
876 that are HIV positive/negative (blue and red respectively). **B)** UMAP visualisation of 33,504
877 lung cells reclustered at a higher resolution to characterise the immune landscape, coloured
878 by cell type. **C)** UMAP visualisation of 33,378 lung cells reclustered at a higher resolution to
879 characterise the stromal landscape, coloured by cell type. To note, cells assigned 'soup'
880 were not able to be clearly defined by canonical cell type markers and were indicative of
881 multiplets/low quality cells. **D)** Volcano plot showing top differentially expressed genes in
882 alveolar macrophages in COVID-19 compared to LRTD with a significant adjusted p-value
883 (<0.05) and a log-fold change of more than 0.5. **E)** Violin plots showing the gene module
884 score across alveolar macrophages in gene sets associated with the gamma, alpha, beta,
885 lambda and TNF response in COVID-19 compared to LRTD. Black lines indicate the median
886 value across all cells, with asterisks to denote the significance level (ns = non-significant,
887 **** = $p <= 0.0001$).
888
889 **Figure 4** | *Integration with Human Lung Cell Atlas Covid19 cohorts highlights dominant T-cell*
890 *macrophage IFN-γ axis in Malawi Covid19 cases*
891 **A)** UMAP visualisation of 147,935 lung cells deriving from integrating cells from Covid19,
892 LRTD and non-LRTD cases from our cohort with cells from the HLCA from non-LRTD, LRTD
893 and Covid19 cases. Clusters are coloured by cell type. **B)** Heatmap showing pathway analysis
894 for differentially expressed genes in our COVID-19 cohort compared to the HLCA COVID-19

895 cohort. Shown are the 50 canonical hallmark gene sets (for list see Supplemental
896 information) coloured by the normalised enrichment score for each cell type. Gene ontology
897 pathways of interest are indicated by arrows (IL6 JAK STAT3 SIGNALING, green, TNFA
898 SIGNALING VIA NFKB, blue, INTERFERON GAMMA RESPONSE, orange). **C)** Dot plot showing
899 the average expression of top differentially expressed genes in the lung alveolar
900 macrophages that contribute the highest in the hallmark gene set "INTERFERON GAMMA
901 RESPONSE" pathway in our COVID-19 cohort compared to the HLCA COVID-19 cohort.
902
903 **Figure 5** | *scRNA-seq of nasal and blood cells: nasal but not blood cells parallel lung IFN-γ*
904 *response.*
905 **A)** UMAP visualisation of 8,098 nasal cells across our cohort, coloured by broad cell types.
906 Outer circos tracks denote the proportion of each cell type across our three disease groups
907 (COVID-19 orange, LRTD blue and No-LRTD green) and whether the cells belong to patients
908 that are HIV positive/negative (blue and red respectively). **B)** UMAP visualisation of 13,350
909 peripheral blood cells across our cohort, coloured by broad cell types. Outer circos tracks
910 denote the proportion of each cell type across our three disease groups (COVID-19 orange,
911 LRTD blue and No-LRTD green) and whether the cells belong to patients that are HIV
912 positive/negative (blue and red respectively). **C-D)** Volcano plots showing top differentially
913 expressed genes in nasal macrophages and T-cells in COVID-19 compared to LRTD with a
914 significant adjusted p-value (<0.05) and a log-fold change of more than 0.5. **E-F)** Volcano
915 plots showing top differentially expressed genes in peripheral blood monocytes and CD4+ T
916 cells respectively in COVID-19 compared to LRTD with a significant adjusted p-value (<0.05)
917 and a log-fold change of more than 0.5.
918
919
920 **Figure 6** | *Spatially resolved cell interaction analysis predicts molecular mechanisms of*
921 *alveolar and endothelial pathology*
922 **A)** Circos plot showing the top 50 differentially expressed interactions upregulated in our
923 COVID-19 cohort compared to LRTD. Segments are coloured by cell type with ligands and
924 receptors labelled on the outside. Direction of the arrows show the senders of
925 communications i.e. expression of ligand, and receiver of communications. Inner tracks on
926 sender segments are coloured by the receiving cell type for ease of interpretation. **B-C)**
927 Heatmaps showing co-localised cell types as shown by the IMC providing insight into
928 potentially interacting cell types in the lung. **D)** Heatmap showing up/down-regulated
929 interactions in COVID-19 compared to LRTD driven by AT2 pneumonocytes to alveolar
930 macrophages. Coloured boxes indicate cell type with the ligand-expressing cell type
931 followed by the receptor-expressing cell type. **E)** Heatmap showing up/down-regulated
932 interactions in COVID-19 compared to LRTD driven by lung alveolar macrophages to lung
933 epithelial cells and interstitial macrophages. Coloured boxes indicate cell type with the
934 ligand-expressing cell type followed by the receptor-expressing cell type. **F)** Heatmap
935 showing up/down-regulated interactions in COVID-19 compared to LRTD driven by lung
936 endothelium to neutrophils. Coloured boxes indicate cell type with the ligand-expressing
937 cell type followed by the receptor-expressing cell type. **G)** Heatmap showing up/down-
938 regulated interactions in COVID-19 compared to LRTD driven by neutrophils to lung
939 endothelium. Coloured boxes indicate cell type with the ligand-expressing cell type followed
940 by the receptor-expressing cell type.
941

942
943
944 **Figure legends — Extended data**
945
946 **Extended data Figure 1 |** *The histopathology of fatal Covid19 versus fatal non-Covid19*
947 *LRTD and non-LRTD in Malawian cases.*
948 Histopathology in the left and right lungs of the 16 cases was scored systematically using
949 pre-defined criteria by two pathologists who were blinded to clinical information. We used
950 identical scoring to a Brazil cohort that we have published on separately. A – C are
951 histograms of the scoring: **A**) Comparsion of Covid19 (n=9) and non-Covid19 fatal lower
952 respiratory tract disease (LRTD) cases (n=5). **B**) Comparison of histological features between
953 HIV+ Covid19 cases (n=5) and HIV- Covid19 cases (n=4). **C**) Comparison of Covid19 cases
954 from Malawi cohort (n=9) with cases from Brazil cohort (n=20). A two sided T-test was used
955 to compare lesion frequencies with no correction for multiple comparisions *=p=<0.05. **D**)
956 PCA of cases split by groups. E) UMAP of same data, including HIV status
957
958 **Extended data Figure 2 |** *Cell atlas and phenotype of cell types identified in the post-mortem*
959 *lung tissue determined by Imaging Mass Cytometry (IMC).*
960 **A**) Phenotype representation of each cell type identified in the lung samples. The heatmap
961 shows the mean expression of each protein marker in the IMC panel in each cell type
962 identified in the post-mortem lung tissue. **B**) Frequency of the immune cell types identified
963 in the post-mortem lung samples by IMC according to clinical groups and according to HIV
964 status within the COVID-19 group. **C**) Frequency of the stromal cell types identified in the
965 post-mortem lung samples by IMC according to clinical groups and according to HIV status
966 within the COVID-19 group. **D**) Frequency and absolute numbers of SARS-CoV-2 Ag+ cells in
967 the myeloid and epithelial compartments, determined by IMC, in the post-mortem lung
968 samples according to HIV status within the COVID-19 group. **E**) Cell type enrichment analysis
969 of the cell populations identified in Malawi lung IMC data. The comparison shown is
970 between COVID-19 versus LRTD cases. To correct for multiple testing, the spatial false
971 discovery rate (FDR) was calculated and only dots with spatialFDR < 0.05 are shown. **F**)
972 Cellular landscape of histopathological lesions based on matched H&E and IMC analysis of
973 post-mortem lung samples from the different clinical groups. The lesions were pooled and
974 the graph shows the average proportion of each cell type in each lesion type. Colour key is
975 as for Fig.2a,b.
976
977 **Extended data Figure 3 |** *Minimal SARS-CoV2 reads in single-cell data of lung, nasal and*
978 *blood cells*
979 **(A)** Lung reference as in Fig 3a. **(B-D)** UMAPs indicate the cells in which we found reads that
980 mapped to the SARS-CoV2 genome, coloured by case. **D)** Table showing absolute cell
981 numbers per case that contain expression of valid UMI to the SARS-CoV2 genome in the
982 lung, peripheral blood and nasal compartment.
983
984 **Extended data figure 4 |** *Lung cell proportions and gene module scores*
985 A-B) Cell type proportion bar plots of lung cell types in A) Immune cells and B) Stromal cells
986 corresponding with Fig 3B and Fig 3C, grouped by disease group. C) Heatmap showing the
987 mean gene module score across cells in gene sets associated with the *alpha, beta, gamma,*

988 *lambda and TNF response*. Cell types have been grouped by COVID-19 and LRTD to show the
989 difference in response and module score values have been scaled between -1 and 1.
990
991 **Extended data Figure 5** | *Heatmap of interferon response genes in lung*
992 Heatmaps showing the log fold change of up/down-regulated interferon response genes
993 taken from immunologic gene sets involved in the immune response. Comparisons include
994 the change in interferon response in cells from the HLCA COVID-19 cohort compared to the
995 control cases **(A)**, our COVID-19 cohort compared to control cases from the HLCA **(B)** and
996 interferon responses from our COVID-19 cohort compared to the HLCA COVID-19 cohort **(C)**.
997
998 **Extended data Figure 6** | *Bulk approaches to explore gene signatures*
999 Heatmaps showing cytokine signatures in different tissues. Values are plotted as z-score
1000 (grey mean not measured). Samples are grouped by their disease type. Luminex data of
1001 Nasal (**A**) and Plasma (**B**). Data were transformed with a log2 and for the visualistion with
1002 ComplexHeatmap in R with a Z-score by gene. For the statistical tests we compared levels of
1003 IFN-y, IL6, IL8, TNF and IL1b in nasal fluid and plasma between the Covid-19 and LTRD
1004 samples using a Welch Two Sample t-test which was non-significant for all comparisons, we
1005 did not correct for multiple comparisons. (**C-E)** Pseudobulk heatmaps showing cytokines
1006 included in the Luminex panel on the transcriptomic level in the peripheral blood, lung and
1007 nasal compartment per patient. As for Luminex we compared levels of IFN-y, IL6, IL8, TNF
1008 and IL1b in nasal, blood and lung cells between the Covid-19 and LTRD samples using a
1009 Welch Two Sample t-test which was non-significant for all comparisons, we did not correct
1010 for multiple comparisons.
1011
1012 **Extended data Fig 7** | *Cell-cell interactions in the IMC datasets*
1013 **(A)** Heatmaps for the non-LRTD group showing co-localised cell types as shown by the IMC
1014 providing insight into potentially interacting cell types in the lung, shown for comparison
1015 with the same data from LRTD cases Fig.5b and Covid19 cases Fig5c (main figures) **(B-D)**
1016 Cellular maps showing the spatial location of specific immune cells and the potential of cell-
1017 cell interactions – highlighting spatially enriched macrophage interactions identified in
1018 Fig.5b (main figure). (**B**) shows interactions between alveolar macrophages (purple),
1019 apoptotic alveolar macrophages (blue) and apoptotic alveolar macrophages (yellow). C)
1020 shows interactions between apoptotic alveolar macrophages (yellow) fibroblast (lilach) and
1021 SARSCoV2+ Epithelial cells (purple) (**D**) shows interactions between activated endothelial
1022 cells (blude) and SARSCoV2+ Neutrophils (green)
1023
1024 **Extended data Table 1 |** *Characteristics of the patients*
1025 Summary table of cases recruited into our study.
1026 Abbreviations:
1027 PMI = post mortem interval in hours
1028 Obese/ Underweight indicates nutritional status, determined by a combination of
1029 abdominal circumference measurements and mid-arm circumference measurements and
1030 based on reference data for men and women in African populations : ↑ = overweight; ↑↑
1031 = obese; ↑↑↑ = morbidly obese; ↓ = underweight; ↓↓ = severely underweight
1032 Pre-morbidity: DM2 = type II diabetes mellitus, HT = hypertension

S.S. to death = symptom start to death, indicating the number of days between the first symptoms consistent with Covid19 (fever, cough, headache etc) and death.
Lung IMC = Imaging Mass Cytometry, Lung sc = lung cell single-cell RNA-seq, nasal sc = Nasal cell single-cell RNA-seq, blood sc = blood cell single-cell RNA-seq, Nasal Lx – Nasal Luminex, is for Multiplexed cytokine array on nasal fluid. A dot for each of these parameters indicates that data are available for that assay for that case.

Extended data Table 2 | *Comparison of cell proportions in IMC data*
The table is divided into three sections. The top section shows the proportion of different immune, stromal and vascular cells in the three groups in the Malawi cohort: Covid19, LRTD and non-LRTD and statistical comparison between the groups. The middle section shows comparison between HIV positive and HIV negative Covid19 cases. The bottom section shows comparison between the three IMC cohorts after integration: Brazil, USA and Malawi.

Extended data Table 3 | *Differential gene expression in single-cell data by cell type*
Differential gene expression analysis results from all cell types in the lung, nasal and blood tissue compartments. The table is organised with each comparison of cell types in the Malawi cohort in Covid-19 compared to LRTD in the three tissues and includes comparisons between lung cells in the Malawi cohort compared to the HLCA cohort. The table contains the average log fold change (avg_log2FC) along with the p-value (p_val) and multiple-test corrected p-values (p_val_adj).

References

1 Regev, A. *et al.* The Human Cell Atlas. *Elife* **6** (2017). https://doi.org/10.7554/eLife.27041

2 Lindeboom, R. G. H., Regev, A. & Teichmann, S. A. Towards a Human Cell Atlas: Taking Notes from the Past. *Trends Genet* **37**, 625-630 (2021). https://doi.org/10.1016/j.tig.2021.03.007

3 Rood, J. E., Maartens, A., Hupalowska, A., Teichmann, S. A. & Regev, A. Impact of the Human Cell Atlas on medicine. *Nat Med* **28**, 2486-2496 (2022). https://doi.org/10.1038/s41591-022-02104-7

4 Majumder, P. P., Mhlanga, M. M. & Shalek, A. K. The Human Cell Atlas and equity: lessons learned. *Nat Med* **26**, 1509-1511 (2020). https://doi.org/10.1038/s41591-020-1100-4

5 Divangahi, M. *et al.* Trained immunity, tolerance, priming and differentiation: distinct immunological processes. *Nat Immunol* **22**, 2-6 (2021). https://doi.org/10.1038/s41590-020-00845-6

6 Mangino, M., Roederer, M., Beddall, M. H., Nestle, F. O. & Spector, T. D. Innate and adaptive immune traits are differentially affected by genetic and environmental factors. *Nat Commun* **8**, 13850 (2017). https://doi.org/10.1038/ncomms13850

7 Delorey, T. M. *et al.* COVID-19 tissue atlases reveal SARS-CoV-2 pathology and cellular targets. *Nature* **595**, 107-113 (2021). https://doi.org/10.1038/s41586-021-03570-8

8 Melms, J. C. *et al.* A molecular single-cell lung atlas of lethal COVID-19. *Nature* **595**, 114-119 (2021). https://doi.org/10.1038/s41586-021-03569-1

9 Ilieva, M., Tschaikowski, M., Vandin, A. & Uchida, S. The current status of gene expression profilings in COVID-19 patients. *Clin Transl Discov* **2**, e104 (2022). https://doi.org/10.1002/ctd2.104

10 Sikkema, L. *et al.* An integrated cell atlas of the lung in health and disease. *Nat Med* **29**, 1563-1577 (2023). https://doi.org/10.1038/s41591-023-02327-2

11 Liao, M. *et al.* Single-cell landscape of bronchoalveolar immune cells in patients with COVID-19. *Nat Med* **26**, 842-844 (2020). https://doi.org/10.1038/s41591-020-0901-9

12 Consortium, C. T. A. *et al.* Single-nuclei characterization of pervasive transcriptional signatures across organs in response to COVID-19. *Elife* **12** (2023). https://doi.org/10.7554/eLife.81090

13 Da Silva Filho, J. L. *et al.* Disease trajectories in hospitalized COVID-19 patients are predicted by clinical and peripheral blood signatures representing distinct lung pathologies. *MedRxiv* (2023). https://doi.org/https://doi.org/10.1101/2023.09.08.23295024

14 Alijotas-Reig, J. *et al.* Immunomodulatory therapy for the management of severe COVID-19. Beyond the anti-viral therapy: A comprehensive review. *Autoimmun Rev* **19**, 102569 (2020). https://doi.org/10.1016/j.autrev.2020.102569

15 Hall, M. W., Joshi, I., Leal, L. & Ooi, E. E. Immune Immunomodulation in Coronavirus Disease 2019 (COVID-19): Strategic Considerations for Personalized Therapeutic Intervention. *Clin Infect Dis* **74**, 144-148 (2022). https://doi.org/10.1093/cid/ciaa904

16 de Jong, S. E. *et al.* Systems analysis and controlled malaria infection in Europeans and Africans elucidate naturally acquired immunity. *Nat Immunol* **22**, 654-665 (2021). https://doi.org/10.1038/s41590-021-00911-7

17 Franklin, B. S. *et al.* Malaria primes the innate immune response due to interferon-gamma induced enhancement of toll-like receptor expression and function. *Proc Natl Acad Sci U S A* **106**, 5789-5794 (2009). https://doi.org/10.1073/pnas.0809742106

18 Guha, R. *et al.* Plasmodium falciparum malaria drives epigenetic reprogramming of human monocytes toward a regulatory phenotype. *PLoS Pathog* **17**, e1009430 (2021). https://doi.org/10.1371/journal.ppat.1009430

19 Breiman, R. F. *et al.* Postmortem investigations and identification of multiple causes of child deaths: An analysis of findings from the Child Health and Mortality Prevention Surveillance (CHAMPS) network. *PLoS Med* **18**, e1003814 (2021). https://doi.org/10.1371/journal.pmed.1003814

20 Ackermann, M. *et al.* Pulmonary Vascular Endothelialitis, Thrombosis, and Angiogenesis in Covid-19. *N Engl J Med* **383**, 120-128 (2020). https://doi.org/10.1056/NEJMoa2015432

21 Borczuk, A. C. *et al.* COVID-19 pulmonary pathology: a multi-institutional autopsy cohort from Italy and New York City. *Mod Pathol* **33**, 2156-2168 (2020). https://doi.org/10.1038/s41379-020-00661-1

22 Duarte-Neto, A. N. *et al.* Ultrasound-Guided Minimally Invasive Tissue Sampling: A Minimally Invasive Autopsy Strategy During the COVID-19 Pandemic in Brazil, 2020. *Clin Infect Dis* **73**, S442-S453 (2021). https://doi.org/10.1093/cid/ciab885

1124 23 Himwaze, C. M. *et al.* Post-mortem examination of Hospital Inpatient COVID-19
1125 Deaths in Lusaka, Zambia - A Descriptive Whole-body Autopsy Series. *Int J Infect Dis*
1126 **108**, 363-369 (2021). https://doi.org/10.1016/j.ijid.2021.06.013
1127 24 Menter, T. *et al.* Postmortem examination of COVID-19 patients reveals diffuse
1128 alveolar damage with severe capillary congestion and variegated findings in lungs
1129 and other organs suggesting vascular dysfunction. *Histopathology* **77**, 198-209
1130 (2020). https://doi.org/10.1111/his.14134
1131 25 Mudenda, V. *et al.* Histopathological Evaluation of Deceased Persons in Lusaka,
1132 Zambia With or Without Coronavirus Disease 2019 (COVID-19) Infection: Results
1133 Obtained From Minimally Invasive Tissue Sampling. *Clin Infect Dis* **73**, S465-S471
1134 (2021). https://doi.org/10.1093/cid/ciab858
1135 26 Xu, Z. *et al.* Pathological findings of COVID-19 associated with acute respiratory
1136 distress syndrome. *Lancet Respir Med* **8**, 420-422 (2020).
1137 https://doi.org/10.1016/S2213-2600(20)30076-X
1138 27 Yao, X. H. *et al.* A cohort autopsy study defines COVID-19 systemic pathogenesis. *Cell*
1139 *Res* **31**, 836-846 (2021). https://doi.org/10.1038/s41422-021-00523-8
1140 28 Dorward, D. A. *et al.* Tissue-Specific Immunopathology in Fatal COVID-19. *Am J Respir*
1141 *Crit Care Med* **203**, 192-201 (2021). https://doi.org/10.1164/rccm.202008-3265OC
1142 29 Knoll, R., Schultze, J. L. & Schulte-Schrepping, J. Monocytes and Macrophages in
1143 COVID-19. *Front Immunol* **12**, 720109 (2021).
1144 https://doi.org/10.3389/fimmu.2021.720109
1145 30 Rendeiro, A. F. *et al.* The spatial landscape of lung pathology during COVID-19
1146 progression. *Nature* **593**, 564-569 (2021). https://doi.org/10.1038/s41586-021-
1147 03475-6
1148 31 Mulder, K. *et al.* Cross-tissue single-cell landscape of human monocytes and
1149 macrophages in health and disease. *Immunity* **54**, 1883-1900 e1885 (2021).
1150 https://doi.org/10.1016/j.immuni.2021.07.007
1151 32 Prasse, A. *et al.* A vicious circle of alveolar macrophages and fibroblasts perpetuates
1152 pulmonary fibrosis via CCL18. *Am J Respir Crit Care Med* **173**, 781-792 (2006).
1153 https://doi.org/10.1164/rccm.200509-1518OC
1154 33 Leclerc, E., Fritz, G., Weibel, M., Heizmann, C. W. & Galichet, A. S100B and S100A6
1155 differentially modulate cell survival by interacting with distinct RAGE (receptor for
1156 advanced glycation end products) immunoglobulin domains. *J Biol Chem* **282**, 31317-
1157 31331 (2007). https://doi.org/10.1074/jbc.M703951200
1158 34 MacDonald, L. *et al.* COVID-19 and RA share an SPP1 myeloid pathway that drives
1159 PD-L1+ neutrophils and CD14+ monocytes. *JCI Insight* **6** (2021).
1160 https://doi.org/10.1172/jci.insight.147413
1161 35 Shan, M. *et al.* Cigarette smoke induction of osteopontin (SPP1) mediates T(H)17
1162 inflammation in human and experimental emphysema. *Sci Transl Med* **4**, 117ra119
1163 (2012). https://doi.org/10.1126/scitranslmed.3003041
1164 36 Sposito, B. *et al.* The interferon landscape along the respiratory tract impacts the
1165 severity of COVID-19. *Cell* **184**, 4953-4968 e4916 (2021).
1166 https://doi.org/10.1016/j.cell.2021.08.016
1167 37 Koeffler, H. P., Ranyard, J., Yelton, L., Billing, R. & Bohman, R. Gamma-interferon
1168 induces expression of the HLA-D antigens on normal and leukemic human myeloid
1169 cells. *Proc Natl Acad Sci U S A* **81**, 4080-4084 (1984).
1170 https://doi.org/10.1073/pnas.81.13.4080

1171 38 Morton, B. *et al.* Distinct clinical and immunological profiles of patients with
1172 evidence of SARS-CoV-2 infection in sub-Saharan Africa. *Nat Commun* **12**, 3554
1173 (2021). https://doi.org/10.1038/s41467-021-23267-w
1174 39 Roukens, A. H. E. *et al.* Prolonged activation of nasal immune cell populations and
1175 development of tissue-resident SARS-CoV-2-specific CD8(+) T cell responses
1176 following COVID-19. *Nat Immunol* **23**, 23-32 (2022). https://doi.org/10.1038/s41590-
1177 021-01095-w
1178 40 Carniel, B. F. *et al.* Pneumococcal colonization impairs mucosal immune responses to
1179 live attenuated influenza vaccine. *JCI Insight* **6** (2021).
1180 https://doi.org/10.1172/jci.insight.141088
1181 41 Bosmuller, H., Matter, M., Fend, F. & Tzankov, A. The pulmonary pathology of
1182 COVID-19. *Virchows Arch* **478**, 137-150 (2021). https://doi.org/10.1007/s00428-021-
1183 03053-1
1184 42 Bilsborrow, J. B., Doherty, E., Tilstam, P. V. & Bucala, R. Macrophage migration
1185 inhibitory factor (MIF) as a therapeutic target for rheumatoid arthritis and systemic
1186 lupus erythematosus. *Expert Opin Ther Targets* **23**, 733-744 (2019).
1187 https://doi.org/10.1080/14728222.2019.1656718
1188 43 Das, A. *et al.* Molecular and immune signatures, and pathological trajectories of fatal
1189 COVID-19 lungs defined by in situ spatial single-cell transcriptome analysis. *J Med*
1190 *Virol* **95**, e29009 (2023). https://doi.org/10.1002/jmv.29009
1191 44 Su, H. C., Jing, H., Zhang, Y. & Casanova, J. L. Interfering with Interferons: A Critical
1192 Mechanism for Critical COVID-19 Pneumonia. *Annu Rev Immunol* **41**, 561-585 (2023).
1193 https://doi.org/10.1146/annurev-immunol-101921-050835
1194 45 Taks, E. J. M., Moorlag, S., Netea, M. G. & van der Meer, J. W. M. Shifting the
1195 Immune Memory Paradigm: Trained Immunity in Viral Infections. *Annu Rev Virol* **9**,
1196 469-489 (2022). https://doi.org/10.1146/annurev-virology-091919-072546
1197 46 Chawana, R. *et al.* Potential of Minimally Invasive Tissue Sampling for Attributing
1198 Specific Causes of Childhood Deaths in South Africa: A Pilot, Epidemiological Study.
1199 *Clin Infect Dis* **69**, S361-S373 (2019). https://doi.org/10.1093/cid/ciz550
1200 47 Taylor, A. W. *et al.* Initial findings from a novel population-based child mortality
1201 surveillance approach: a descriptive study. *Lancet Glob Health* **8**, e909-e919 (2020).
1202 https://doi.org/10.1016/S2214-109X(20)30205-9
1203 48 Li, Y. *et al.* Global, regional, and national disease burden estimates of acute lower
1204 respiratory infections due to respiratory syncytial virus in children younger than 5
1205 years in 2019: a systematic analysis. *Lancet* **399**, 2047-2064 (2022).
1206 https://doi.org/10.1016/S0140-6736(22)00478-0
1207 49 . (!!! INVALID CITATION !!! 13,20-27,49,50).
1208 50 Lu, P. *et al.* IMC-Denoise: a content aware denoising pipeline to enhance Imaging
1209 Mass Cytometry. *Nat Commun* **14**, 1601 (2023). https://doi.org/10.1038/s41467-
1210 023-37123-6
1211 51 Geuenich, M. J. *et al.* Automated assignment of cell identity from single-cell
1212 multiplexed imaging and proteomic data. *Cell Syst* **12**, 1173-1186 e1175 (2021).
1213 https://doi.org/10.1016/j.cels.2021.08.012
1214 52 Wolf, F. A., Angerer, P. & Theis, F. J. SCANPY: large-scale single-cell gene expression
1215 data analysis. *Genome Biol* **19**, 15 (2018). https://doi.org/10.1186/s13059-017-1382-
1216 0

1217 53 Levine, J. H. *et al.* Data-Driven Phenotypic Dissection of AML Reveals Progenitor-like
1218 Cells that Correlate with Prognosis. *Cell* **162**, 184-197 (2015).
1219 https://doi.org/10.1016/j.cell.2015.05.047
1220 54 Buttner, M., Ostner, J., Muller, C. L., Theis, F. J. & Schubert, B. scCODA is a Bayesian
1221 model for compositional single-cell data analysis. *Nat Commun* **12**, 6876 (2021).
1222 https://doi.org/10.1038/s41467-021-27150-6
1223 55 Dann, E., Henderson, N. C., Teichmann, S. A., Morgan, M. D. & Marioni, J. C.
1224 Differential abundance testing on single-cell data using k-nearest neighbor graphs.
1225 *Nat Biotechnol* **40**, 245-253 (2022). https://doi.org/10.1038/s41587-021-01033-z
1226 56 Palla, G. *et al.* Squidpy: a scalable framework for spatial omics analysis. *Nat Methods*
1227 **19**, 171-178 (2022). https://doi.org/10.1038/s41592-021-01358-2
1228 57 Gayoso, A. *et al.* A Python library for probabilistic analysis of single-cell omics data.
1229 *Nat Biotechnol* **40**, 163-166 (2022). https://doi.org/10.1038/s41587-021-01206-w
1230 58 Travaglini, K. J. *et al.* A molecular cell atlas of the human lung from single-cell RNA
1231 sequencing. *Nature* **587**, 619-625 (2020). https://doi.org/10.1038/s41586-020-2922-
1232 4
1233 59 Heaton, H. *et al.* Souporcell: robust clustering of single-cell RNA-seq data by
1234 genotype without reference genotypes. *Nat Methods* **17**, 615-620 (2020).
1235 https://doi.org/10.1038/s41592-020-0820-1
1236 60 Hao, Y. *et al.* Integrated analysis of multimodal single-cell data. *Cell* **184**, 3573-3587
1237 e3529 (2021). https://doi.org/10.1016/j.cell.2021.04.048
1238

Fig 1

A

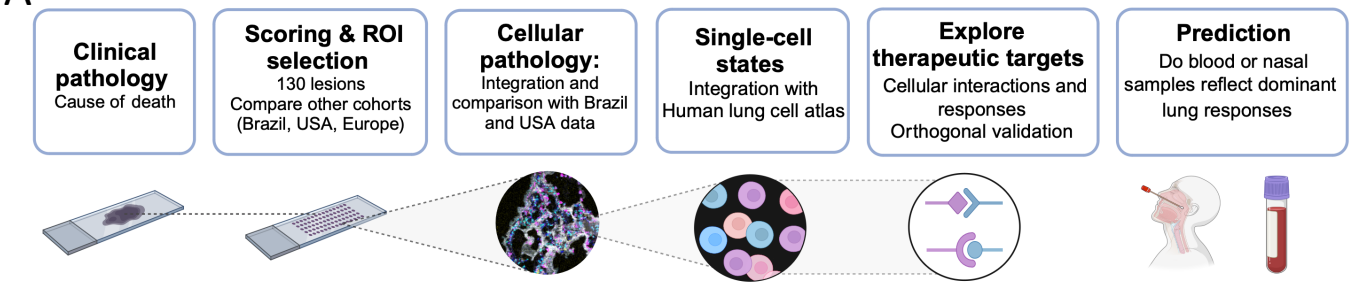

B

Cohort	Group	N=	Age	SS to death	%HIV	Path	Sys. Hist	IMC	lung sc	nasal sc	blood sc
Malawi	Covid19	**9**	56 (48-72)	7 (1-20)	56	9	9	9	5	5	4
	LRTD	**5**	60 (49-60)	10 (5-17)	60	5	5	3	3	2	2
	No LRTD	**2**	51.5 (51-52)	3 (2-4)	50	2	2	2	1	1	1

Other cohorts	Group	N=	Age	SS to death	%HIV	Path	Sys. Hist	IMC	lung sc	nasal sc	blood sc
Brazil (De Silva Filho et al.)	Covid19	**30**	61 (27-88)	18 (5-43)	0	30	30	11			
USA/Euro (Borczuk et al.)	Covid19	**65**	73 (30-96)	11 (5-27)	3	65					
USA-IMC (Rendeiro et al.)	Covid19	**10**	64 (52-75)	25 (1-49)	0			10			
Human lung cell atlas	Covid19	**60**	21-77	NR	NR				60		
(Sikkema et al.)	LRTD	**13**	NR	NR	NR				13		
	No LRTD	**178**	0 - 81	NR	NR				178		

C

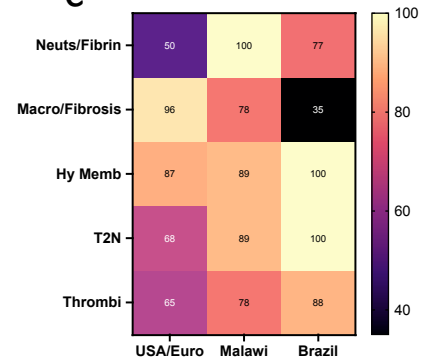

Fig 2

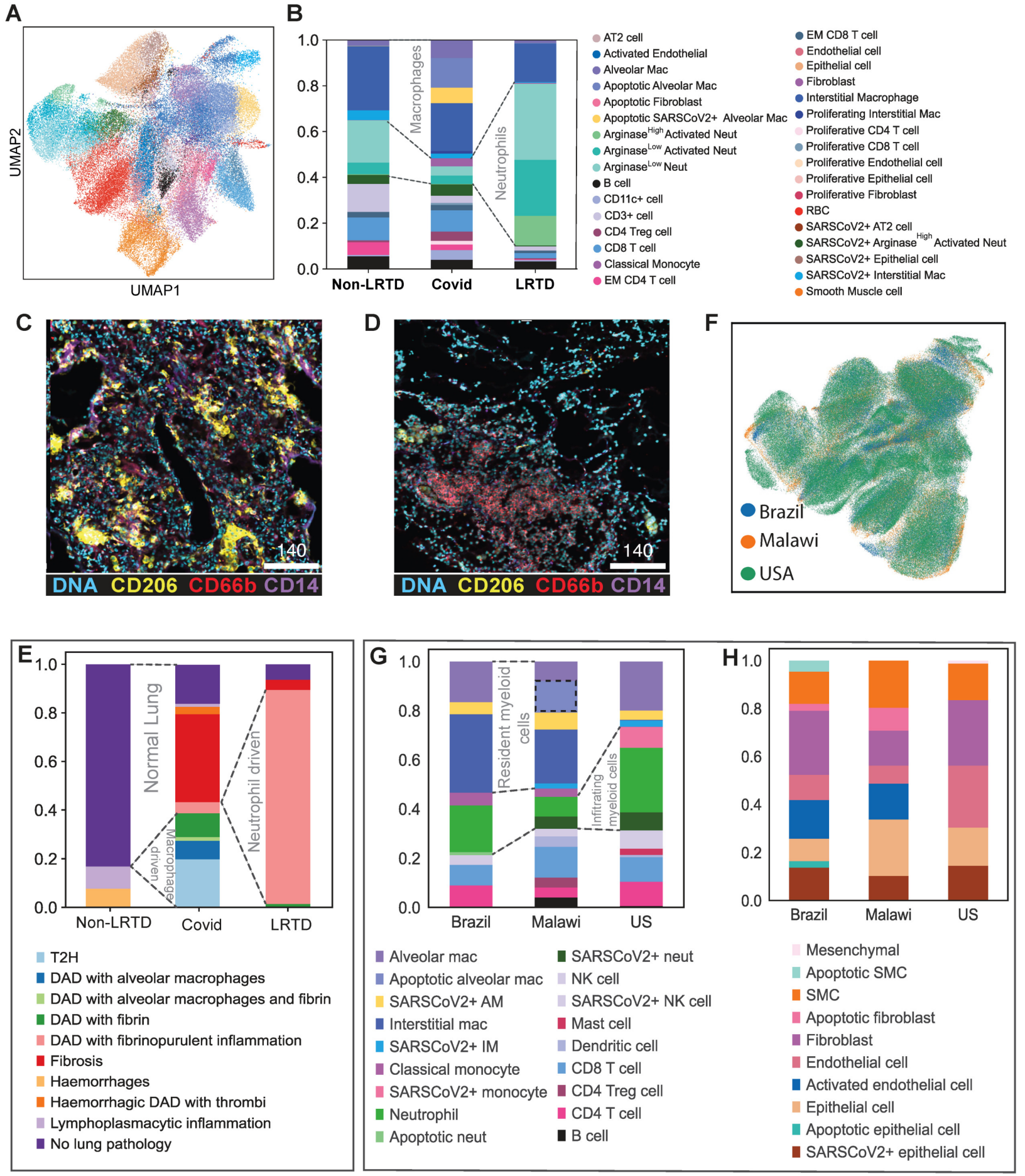
A
UMAP2
UMAP1
B
Macrophages
Neutrophils
Non-LRTD
Covid
LRTD
AT2 cell
Activated Endothelial
Alveolar Mac
Apoptotic Alveolar Mac
Apoptotic Fibroblast
Apoptotic SARSCoV2+ Alveolar Mac
Arginase High Activated Neut
Arginase Low Activated Neut
Arginase Low Neut
B cell
CD11c+ cell
CD3+ cell
CD4 Treg cell
CD8 T cell
Classical Monocyte
EM CD4 T cell
EM CD8 T cell
Endothelial cell
Epithelial cell
Fibroblast
Interstitial Macrophage
Proliferating Interstitial Mac
Proliferative CD4 T cell
Proliferative CD8 T cell
Proliferative Endothelial cell
Proliferative Epithelial cell
Proliferative Fibroblast
RBC
SARSCoV2+ AT2 cell
SARSCoV2+ Arginase High Activated Neut
SARSCoV2+ Epithelial cell
SARSCoV2+ Interstitial Mac
Smooth Muscle cell
C
140
DNA CD206 CD66b CD14
D
140
DNA CD206 CD66b CD14
F
Brazil
Malawi
USA
E
Normal Lung
Macrophage driven
Neutrophil driven
Non-LRTD
Covid
LRTD
T2H
DAD with alveolar macrophages
DAD with alveolar macrophages and fibrin
DAD with fibrin
DAD with fibrinopurulent inflammation
Fibrosis
Haemorrhages
Haemorrhagic DAD with thrombi
Lymphoplasmacytic inflammation
No lung pathology
G
Resident myeloid cells
Infiltrating myeloid cells
Brazil
Malawi
US
Alveolar mac
Apoptotic alveolar mac
SARSCoV2+ AM
Interstitial mac
SARSCoV2+ IM
Classical monocyte
SARSCoV2+ monocyte
Neutrophil
Apoptotic neut
SARSCoV2+ neut
NK cell
SARSCoV2+ NK cell
Mast cell
Dendritic cell
CD8 T cell
CD4 Treg cell
CD4 T cell
B cell
H
Brazil
Malawi
US
Mesenchymal
Apoptotic SMC
SMC
Apoptotic fibroblast
Fibroblast
Endothelial cell
Activated endothelial cell
Epithelial cell
Apoptotic epithelial cell
SARSCoV2+ epithelial cell

Fig 3

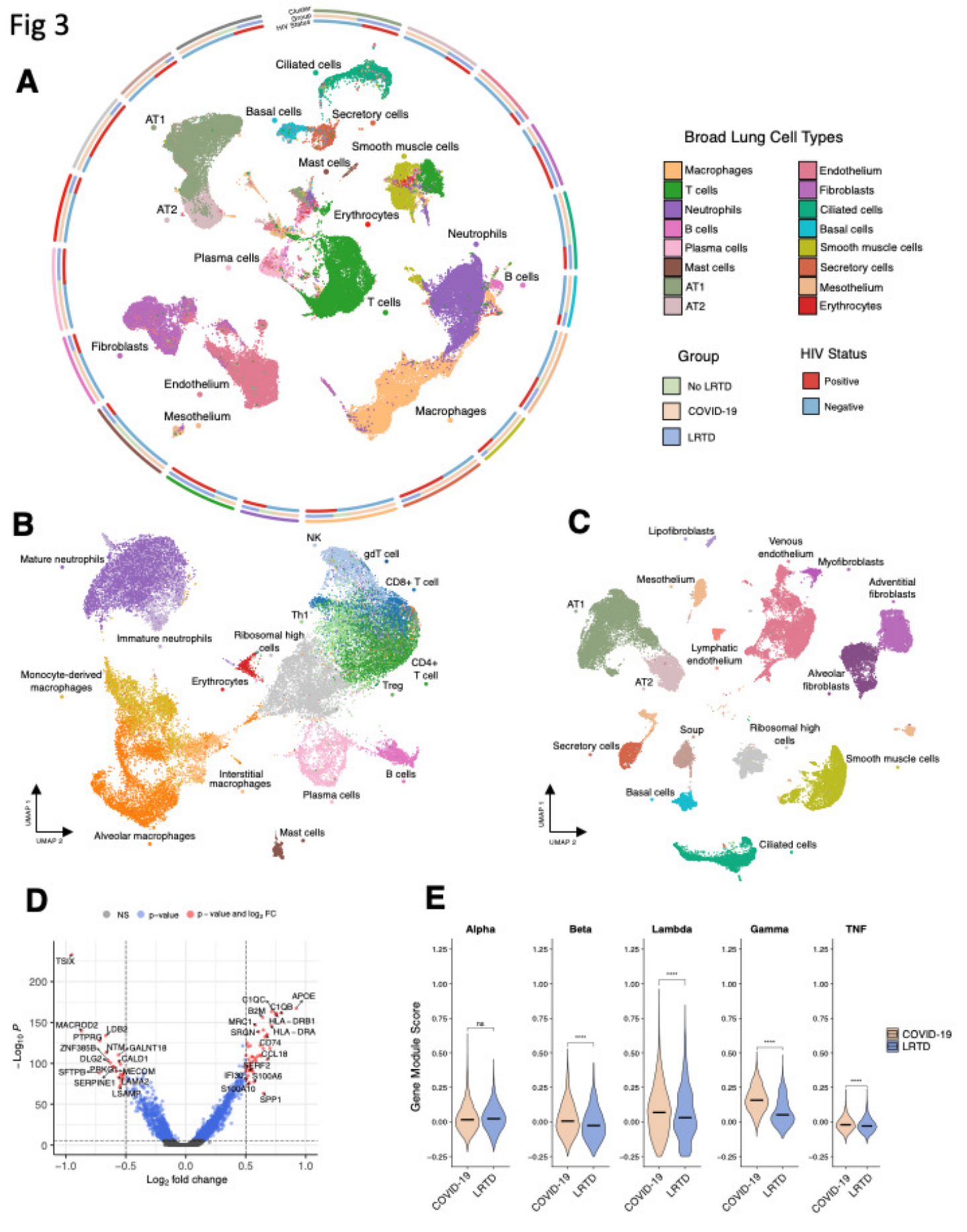
A
Cluster
Group
HIV Status
Ciliated cells
Basal cells
Secretory cells
AT1
Smooth muscle cells
Mast cells
AT2
Erythrocytes
Neutrophils
Plasma cells
B cells
T cells
Fibroblasts
Endothelium
Mesothelium
Macrophages
Broad Lung Cell Types
Macrophages
T cells
Neutrophils
B cells
Plasma cells
Mast cells
AT1
AT2
Endothelium
Fibroblasts
Ciliated cells
Basal cells
Smooth muscle cells
Secretory cells
Mesothelium
Erythrocytes
Group
No LRTD
COVID-19
LRTD
HIV Status
Positive
Negative
B
Mature neutrophils
NK
gdT cell
CD8+ T cell
Th1
Immature neutrophils
Ribosomal high cells
CD4+ T cell
Monocyte-derived macrophages
Erythrocytes
Treg
Interstitial macrophages
B cells
Plasma cells
Alveolar macrophages
Mast cells
UMAP 1
UMAP 2
C
Lipofibroblasts
Venous endothelium
Myofibroblasts
Mesothelium
Adventitial fibroblasts
AT1
Lymphatic endothelium
AT2
Alveolar fibroblasts
Soup
Ribosomal high cells
Secretory cells
Smooth muscle cells
Basal cells
Ciliated cells
UMAP 1
UMAP 2
D
NS
p-value
p-value and log2 FC
TSIX
APOE
C1QC
C1QB
B2M
MRC1
HLA-DRB1
SRGN
HLA-DRA
CD74
CCL18
SERF2
IFI30
S100A6
S100A10
SPP1
MACROD2
LDB2
PTPRG
ZNF385B
NTM
GALNT18
DLG2
GALD1
SFTPB
PBKCI
MECOM
SERPINE1
LAMA2
LSAMP
−Log10 P
Log2 fold change
E
Alpha
Beta
Lambda
Gamma
TNF
Gene Module Score
COVID-19
LRTD
ns
****

Fig 4

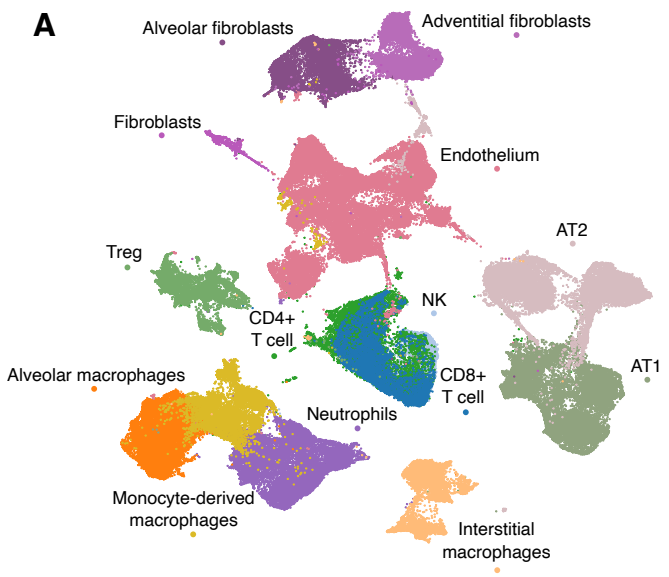
A
Alveolar fibroblasts
Adventitial fibroblasts
Fibroblasts
Endothelium
AT2
Treg
NK
CD4+
T cell
CD8+
T cell
AT1
Alveolar macrophages
Neutrophils
Monocyte-derived
macrophages
Interstitial
macrophages

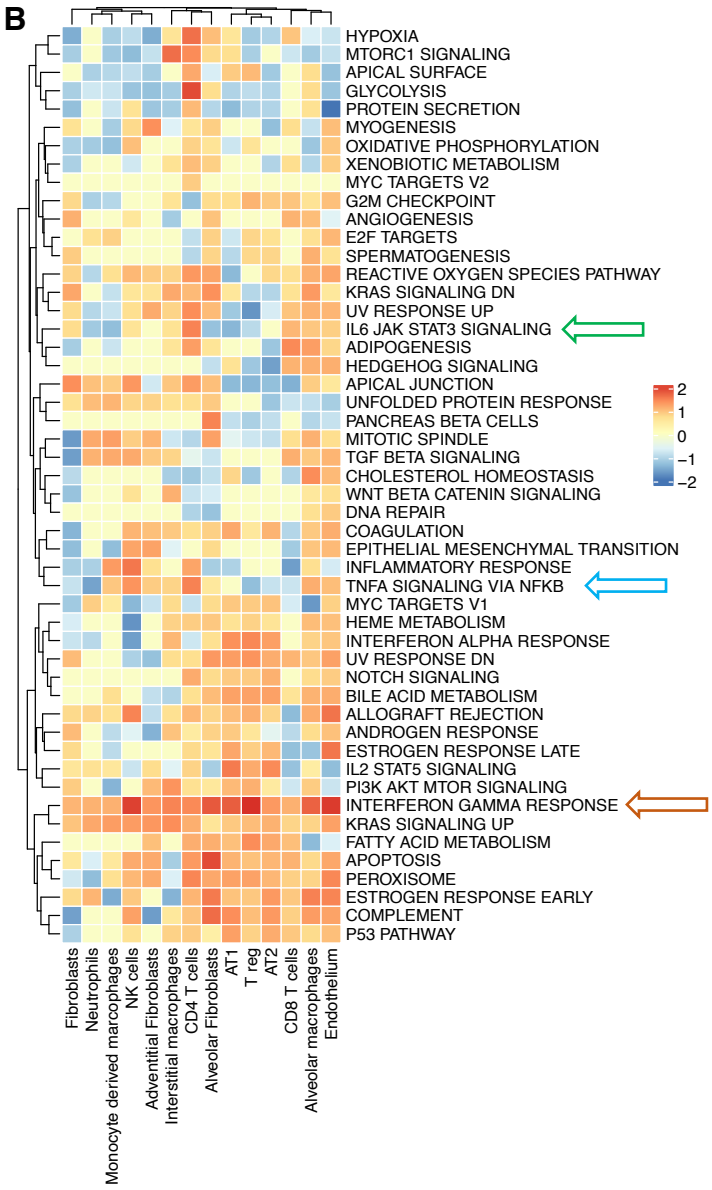
B
HYPOXIA
MTORC1 SIGNALING
APICAL SURFACE
GLYCOLYSIS
PROTEIN SECRETION
MYOGENESIS
OXIDATIVE PHOSPHORYLATION
XENOBIOTIC METABOLISM
MYC TARGETS V2
G2M CHECKPOINT
ANGIOGENESIS
E2F TARGETS
SPERMATOGENESIS
REACTIVE OXYGEN SPECIES PATHWAY
KRAS SIGNALING DN
UV RESPONSE UP
IL6 JAK STAT3 SIGNALING
ADIPOGENESIS
HEDGEHOG SIGNALING
APICAL JUNCTION
UNFOLDED PROTEIN RESPONSE
PANCREAS BETA CELLS
MITOTIC SPINDLE
TGF BETA SIGNALING
CHOLESTEROL HOMEOSTASIS
WNT BETA CATENIN SIGNALING
DNA REPAIR
COAGULATION
EPITHELIAL MESENCHYMAL TRANSITION
INFLAMMATORY RESPONSE
TNFA SIGNALING VIA NFKB
MYC TARGETS V1
HEME METABOLISM
INTERFERON ALPHA RESPONSE
UV RESPONSE DN
NOTCH SIGNALING
BILE ACID METABOLISM
ALLOGRAFT REJECTION
ANDROGEN RESPONSE
ESTROGEN RESPONSE LATE
IL2 STAT5 SIGNALING
PI3K AKT MTOR SIGNALING
INTERFERON GAMMA RESPONSE
KRAS SIGNALING UP
FATTY ACID METABOLISM
APOPTOSIS
PEROXISOME
ESTROGEN RESPONSE EARLY
COMPLEMENT
P53 PATHWAY
2
1
0
−1
−2
Fibroblasts
Neutrophils
Monocyte derived marcophages
NK cells
Adventitial Fibroblasts
Interstitial macrophages
CD4 T cells
Alveolar Fibroblasts
AT1
T reg
AT2
CD8 T cells
Alveolar macrophages
Endothelium

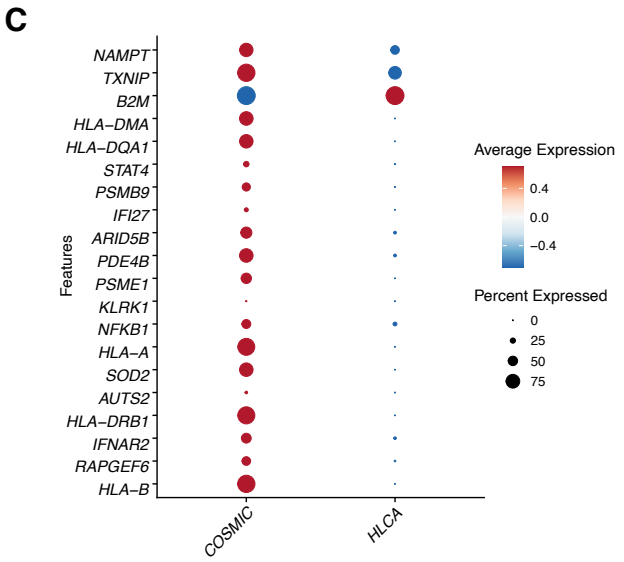
C
NAMPT
TXNIP
B2M
HLA−DMA
HLA−DQA1
STAT4
PSMB9
IFI27
ARID5B
PDE4B
PSME1
KLRK1
NFKB1
HLA−A
SOD2
AUTS2
HLA−DRB1
IFNAR2
RAPGEF6
HLA−B
Features
COSMIC
HLCA
Average Expression
0.4
0.0
−0.4
Percent Expressed
0
25
50
75

Fig 5

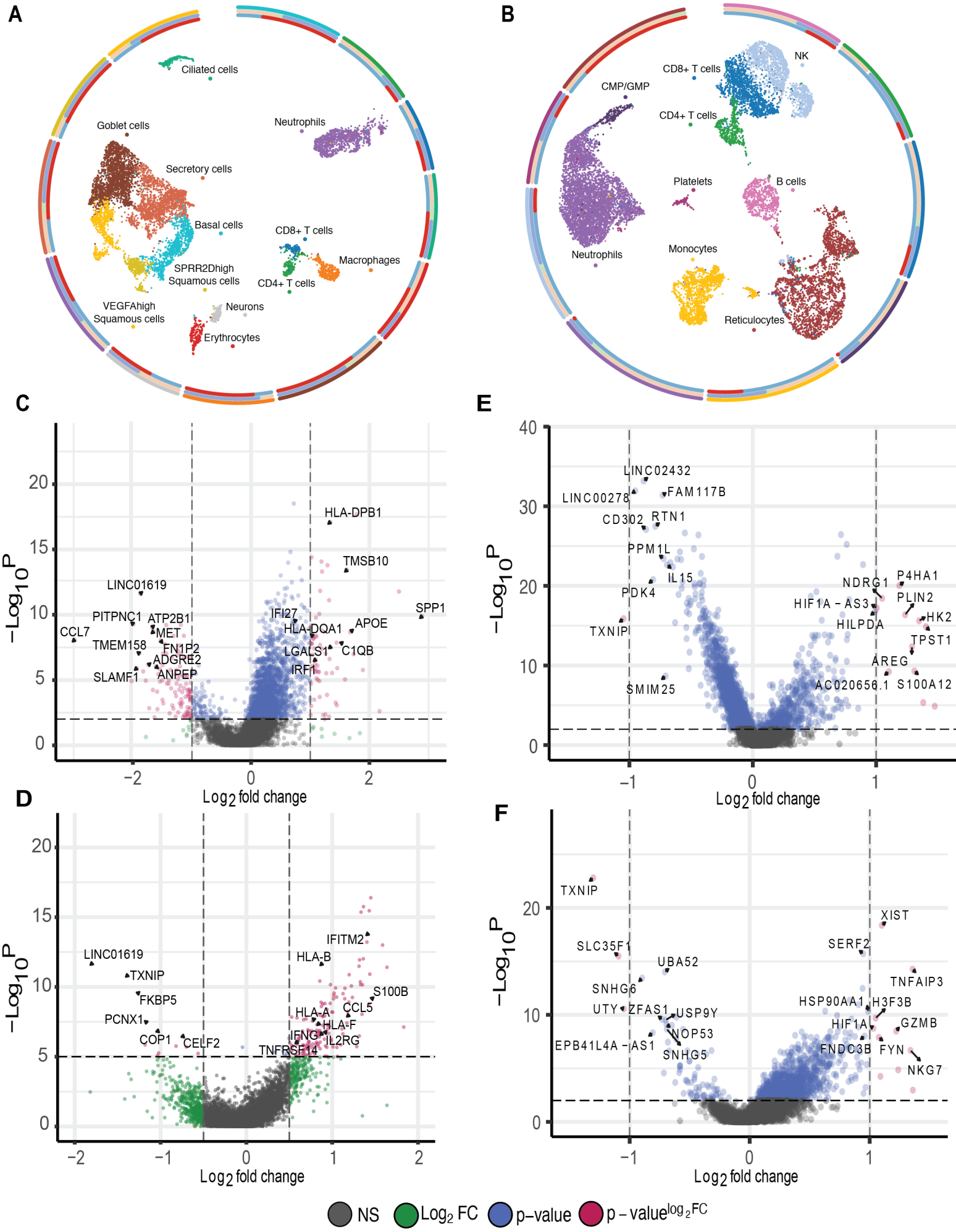
A
Ciliated cells
Goblet cells
Neutrophils
Secretory cells
Basal cells
CD8+ T cells
Macrophages
SPRR2Dhigh Squamous cells
CD4+ T cells
VEGFAhigh Squamous cells
Neurons
Erythrocytes
B
NK
CD8+ T cells
CMP/GMP
CD4+ T cells
Platelets
B cells
Neutrophils
Monocytes
Reticulocytes
C
HLA-DPB1
TMSB10
LINC01619
SPP1
PITPNC1
ATP2B1
IFI27
APOE
CCL7
MET
HLA-DQA1
TMEM158
FN1P2
C1QB
ADGRE2
LGALS1
SLAMF1
ANPEP
IRF1
$-Log_{10}P$
Log_2 fold change
D
IFITM2
LINC01619
HLA-B
TXNIP
S100B
FKBP5
CCL5
HLA-A
PCNX1
HLA-F
IFNG
IL2RG
COP1
CELF2
TNFRSF14
$-Log_{10}P$
Log_2 fold change
E
LINC02432
LINC00278
FAM117B
CD302
RTN1
PPM1L
IL15
PDK4
NDRG1
P4HA1
HIF1A-AS3
PLIN2
HILPDA
HK2
TXNIP
TPST1
AREG
SMIM25
AC020656.1
S100A12
$-Log_{10}P$
Log_2 fold change
F
TXNIP
XIST
SLC35F1
SERF2
UBA52
TNFAIP3
SNHG6
HSP90AA1
H3F3B
UTY
ZFAS1
USP9Y
HIF1A
GZMB
NOP53
EPB41L4A-AS1
SNHG5
FNDC3B
FYN
NKG7
$-Log_{10}P$
Log_2 fold change
NS
Log_2 FC
p-value
p-value^{log_2FC}

Fig 6

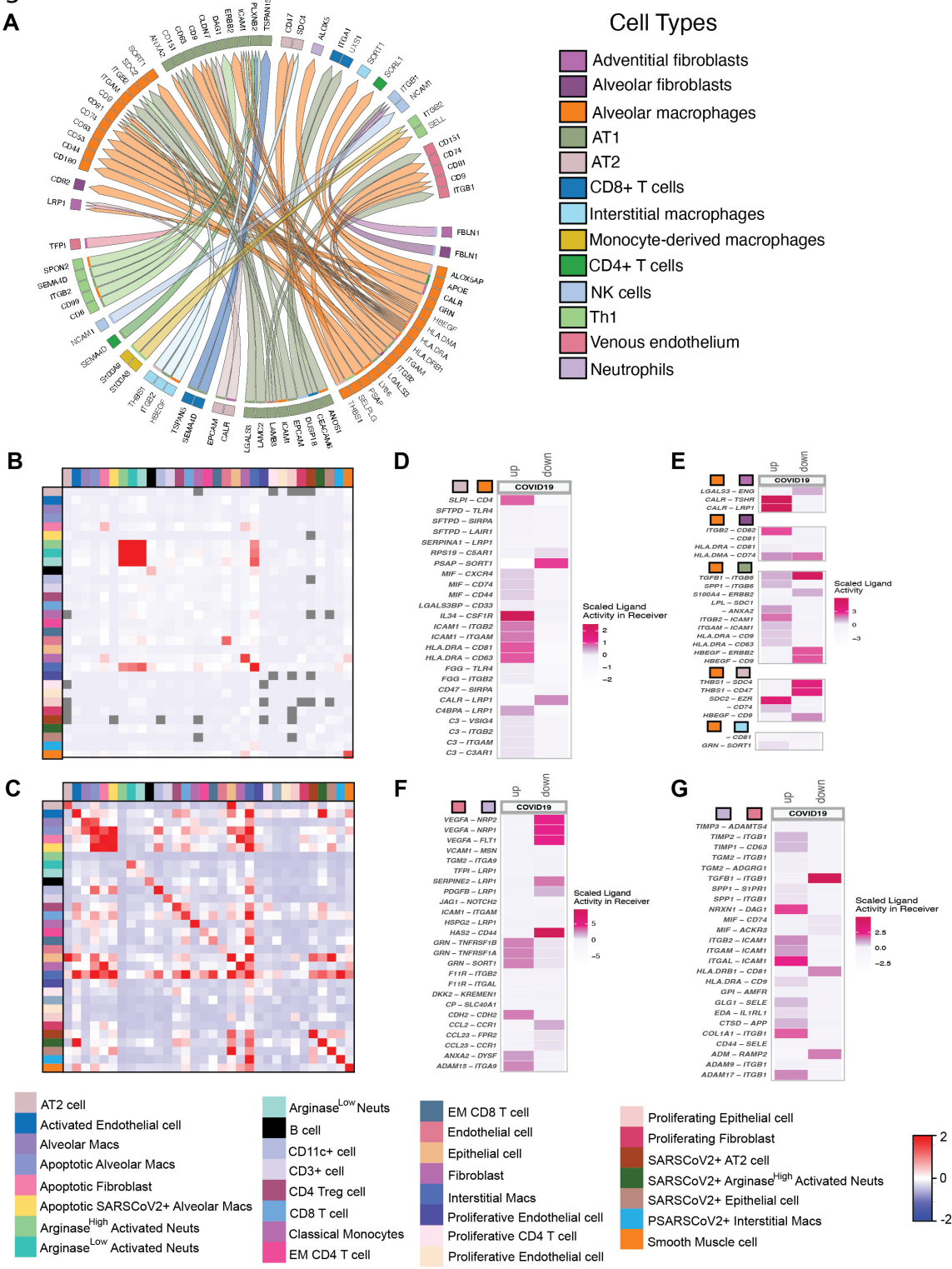
A
Cell Types
Adventitial fibroblasts
Alveolar fibroblasts
Alveolar macrophages
AT1
AT2
CD8+ T cells
Interstitial macrophages
Monocyte-derived macrophages
CD4+ T cells
NK cells
Th1
Venous endothelium
Neutrophils
B
C
D
E
F
G
up
down
COVID19
Scaled Ligand Activity in Receiver
Scaled Ligand Activity
AT2 cell
Activated Endothelial cell
Alveolar Macs
Apoptotic Alveolar Macs
Apoptotic Fibroblast
Apoptotic SARSCoV2+ Alveolar Macs
Arginase High Activated Neuts
Arginase Low Activated Neuts
Arginase Low Neuts
B cell
CD11c+ cell
CD3+ cell
CD4 Treg cell
CD8 T cell
Classical Monocytes
EM CD4 T cell
EM CD8 T cell
Endothelial cell
Epithelial cell
Fibroblast
Interstitial Macs
Proliferative Endothelial cell
Proliferative CD4 T cell
Proliferative Endothelial cell
Proliferating Epithelial cell
Proliferating Fibroblast
SARSCoV2+ AT2 cell
SARSCoV2+ Arginase High Activated Neuts
SARSCoV2+ Epithelial cell
PSARSCoV2+ Interstitial Macs
Smooth Muscle cell

Extended data Fig. 1

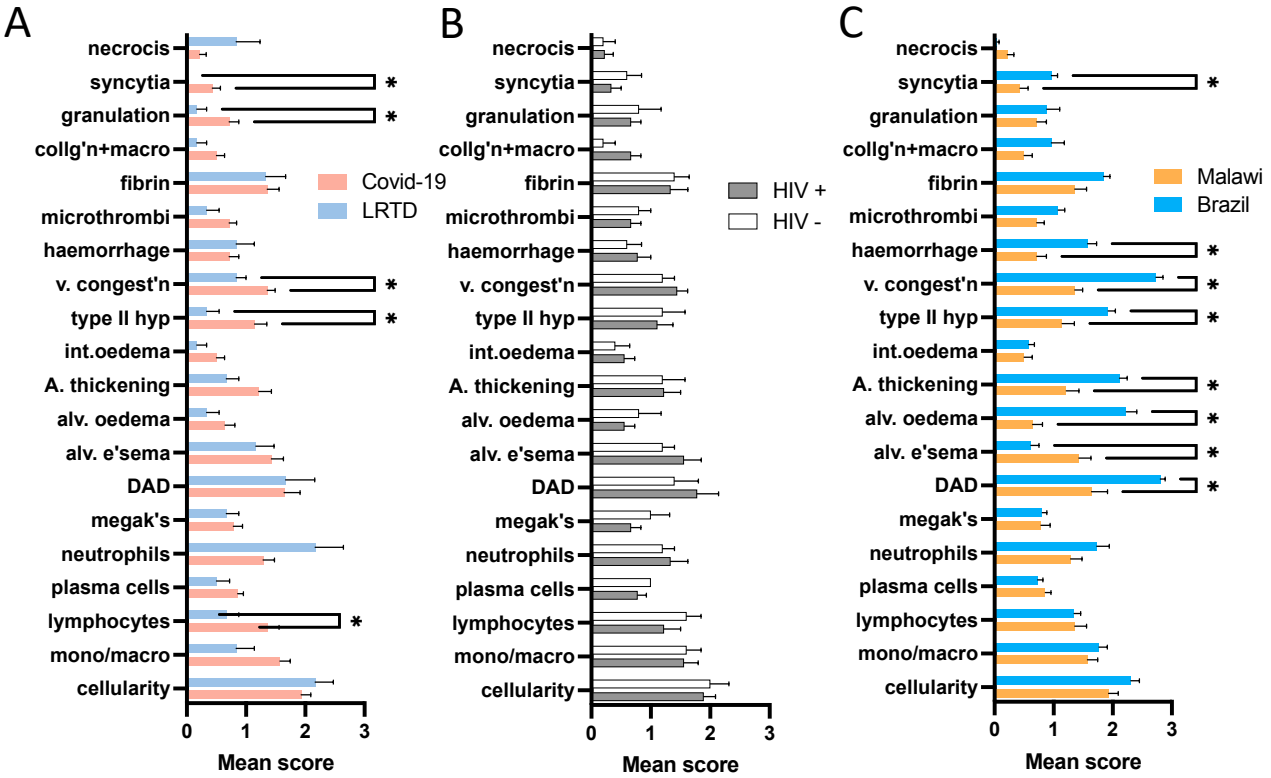

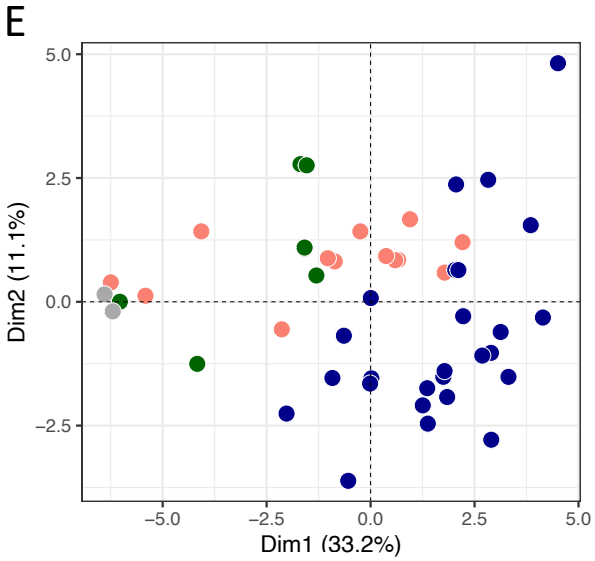

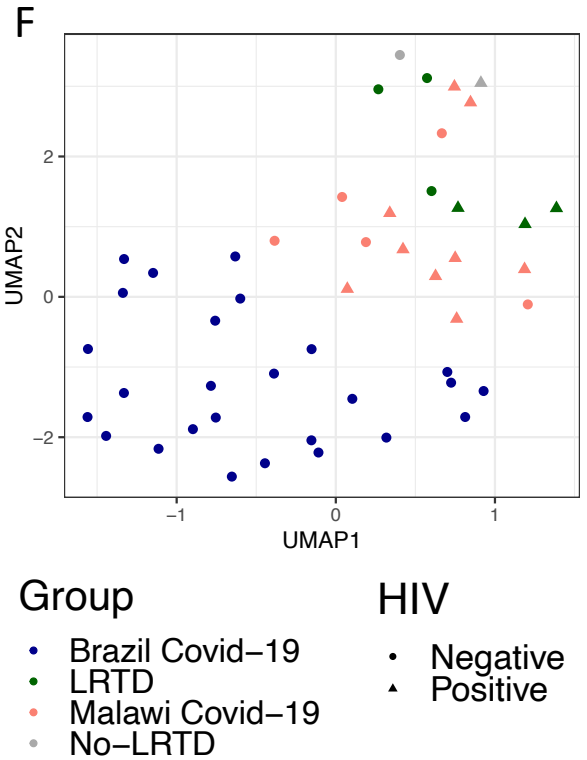

Extended data figure 2:

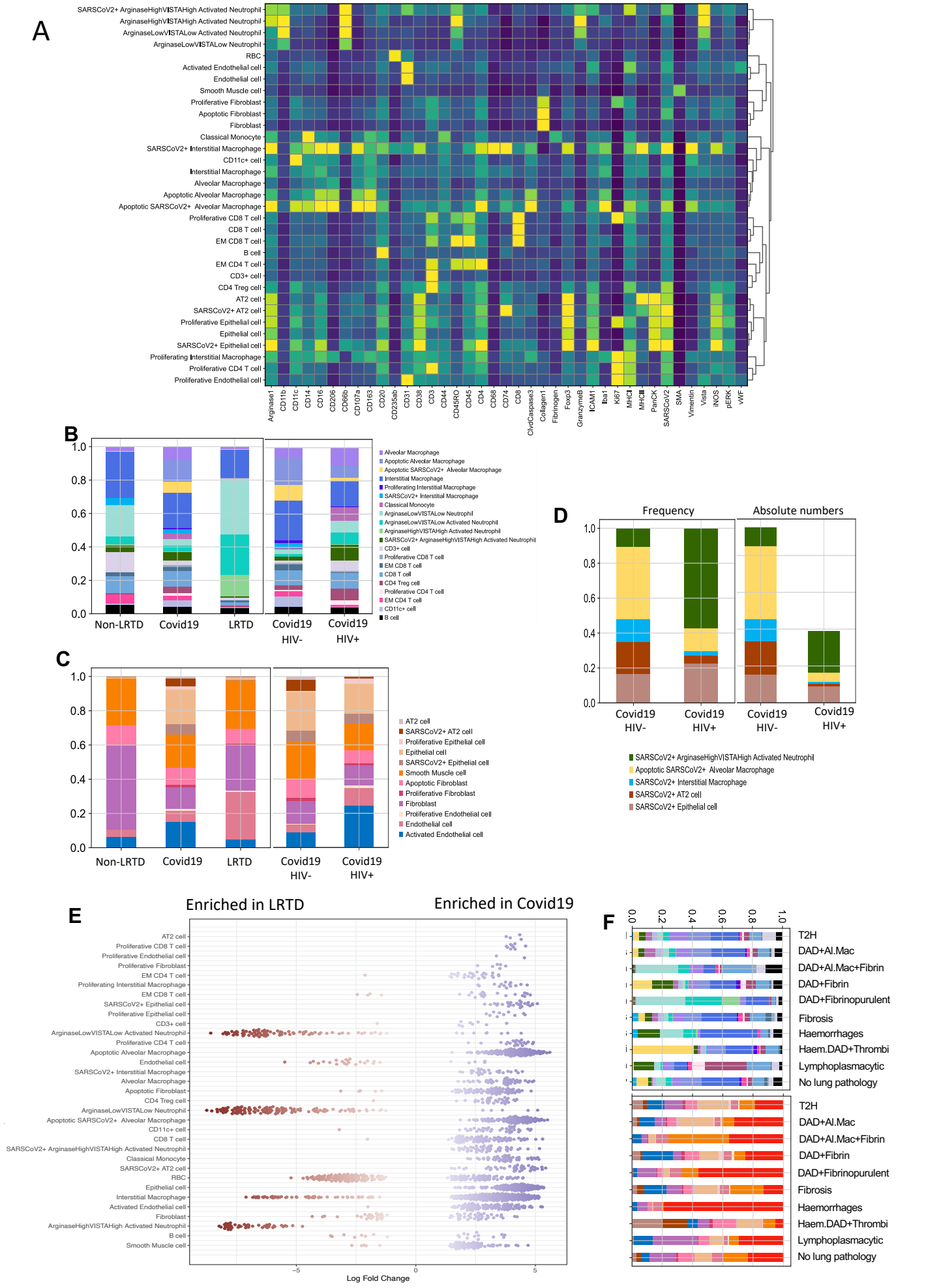

Extended data figure 3:

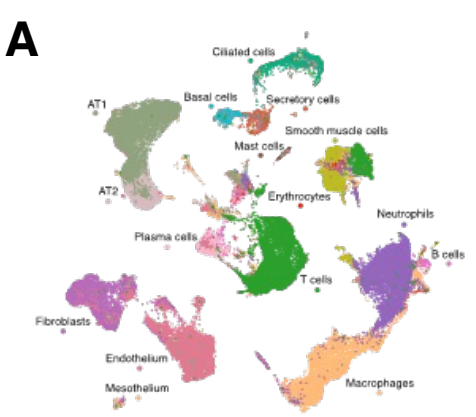

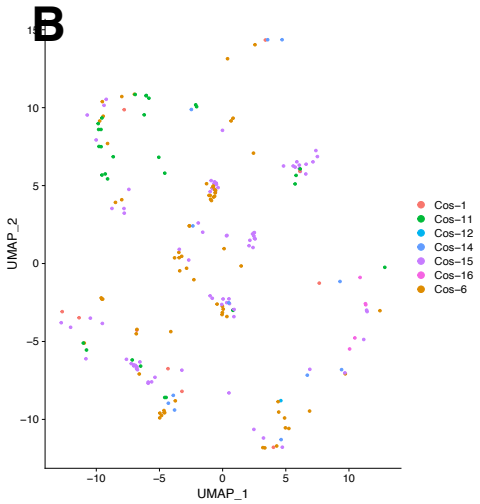

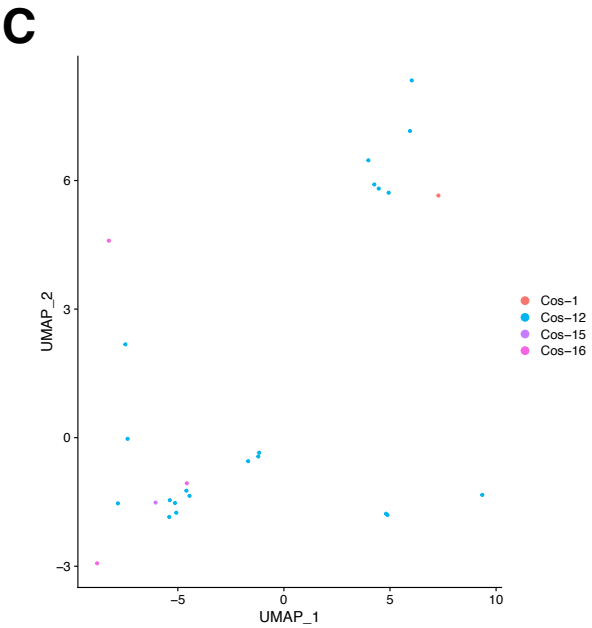

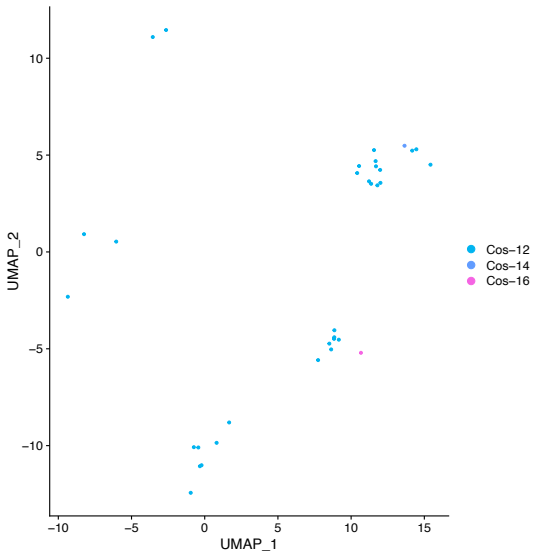

D

Tissue	Lung	Blood	Nasal	Total
Cos1	10	1	X	11
Cos6	69	X	X	69
Cos11	30	X	X	30
Cos12	1	21	32	54
Cos14	12	X	1	13
Cos15	87	1	X	88
Cos16	5	3	1	9
Total	214	26	34	274

Extended data Fig 4:

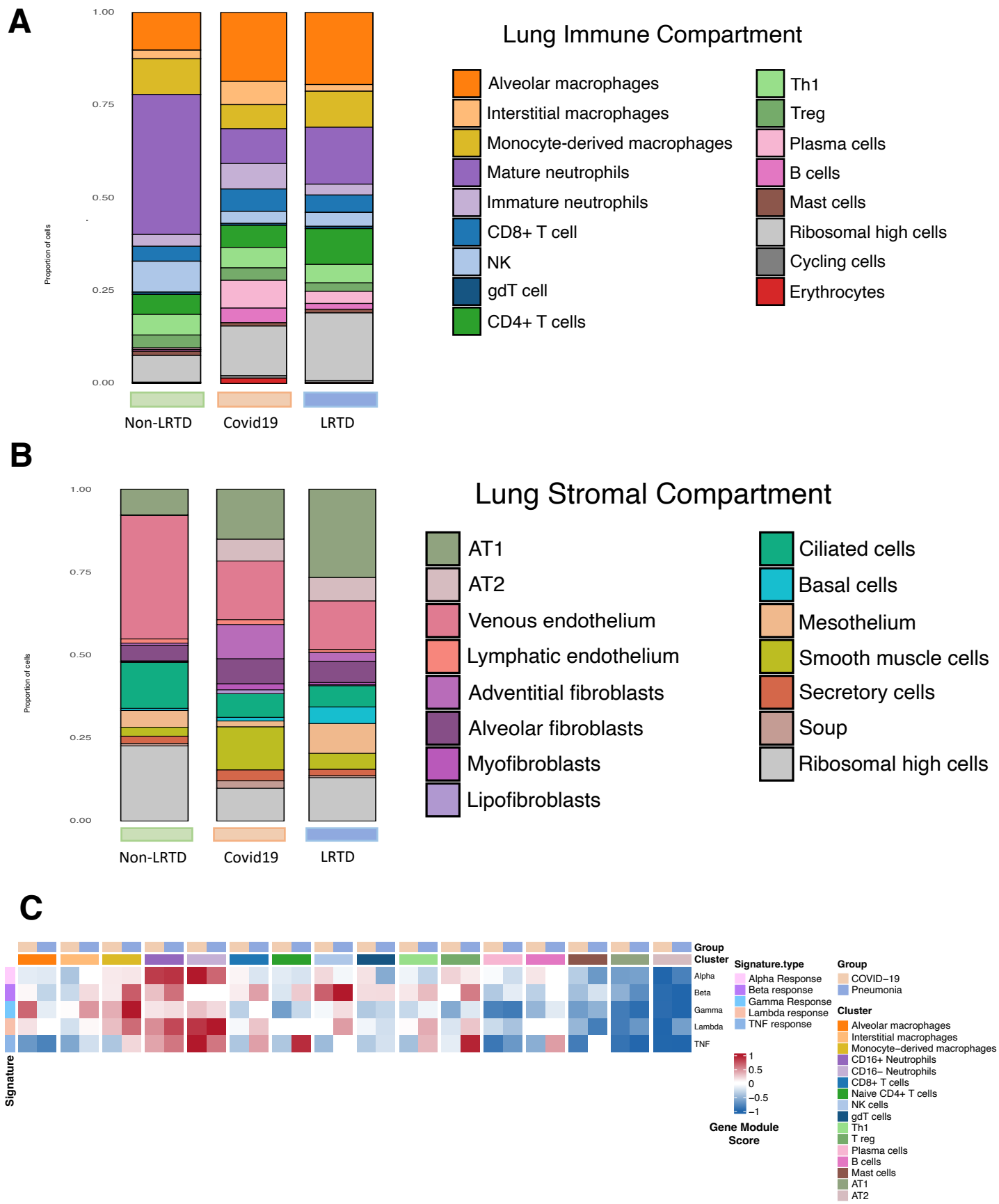

Extended data Fig 5:

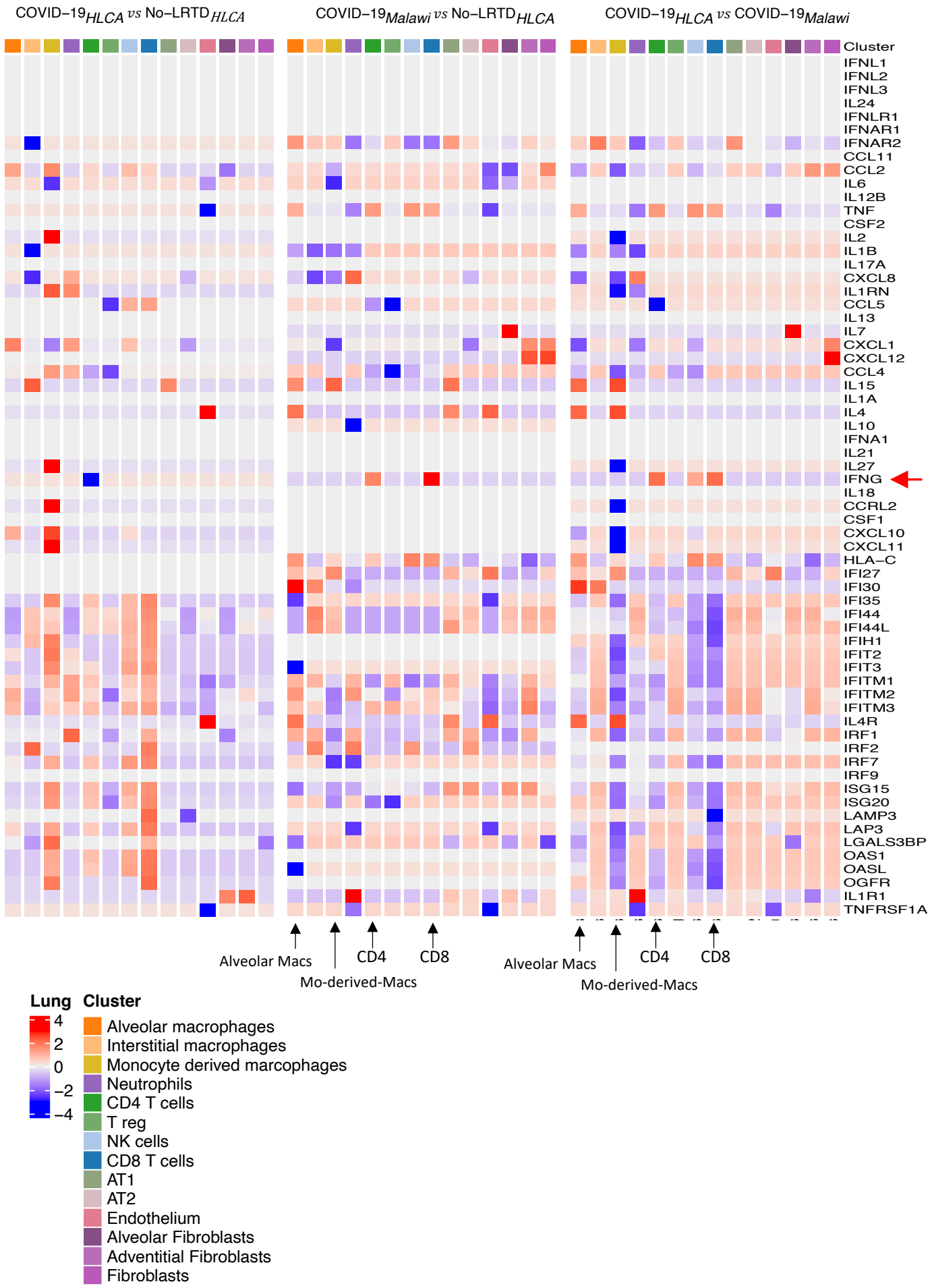

Extended data Fig 6:

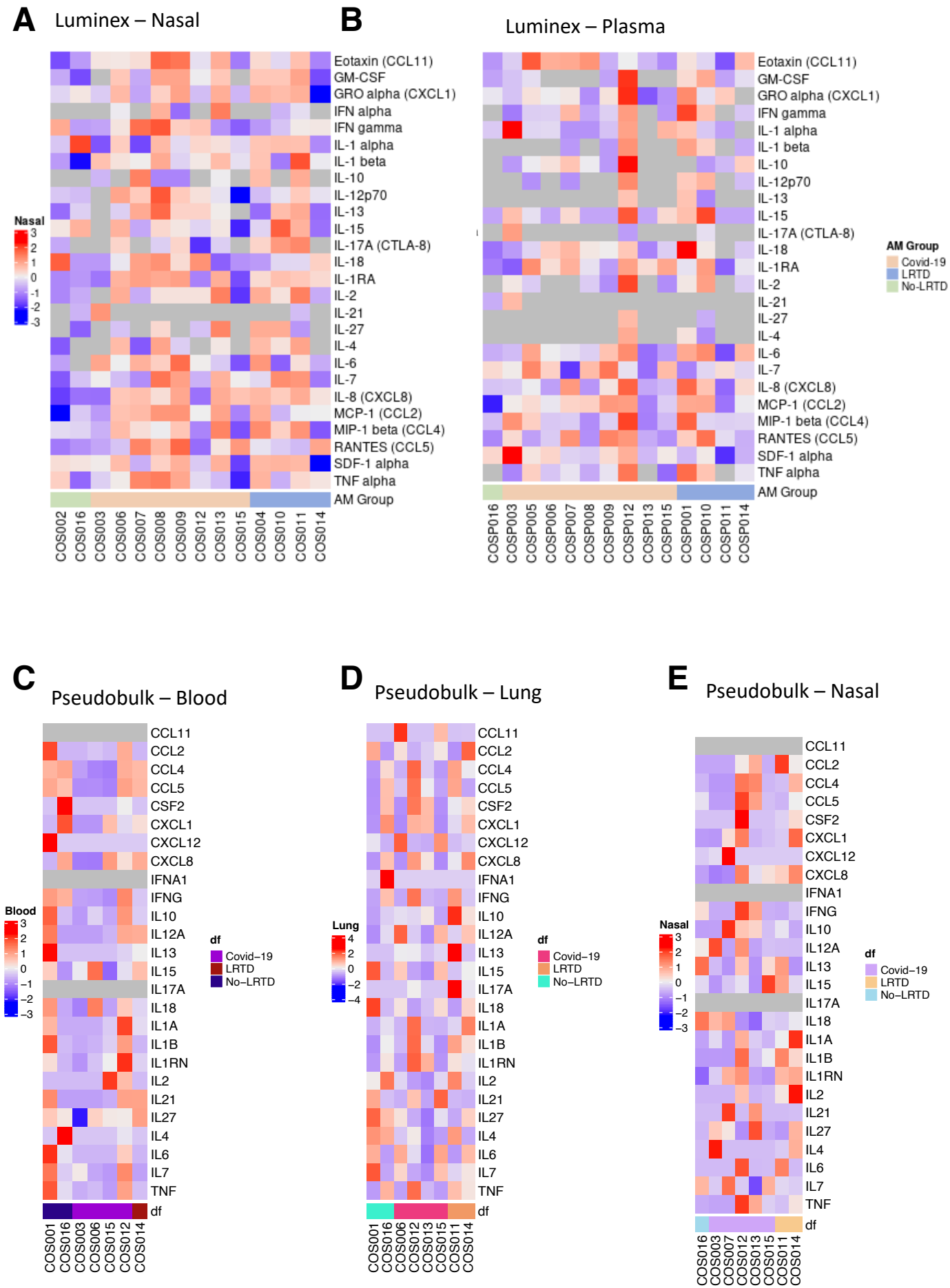

Extended data Fig. 7

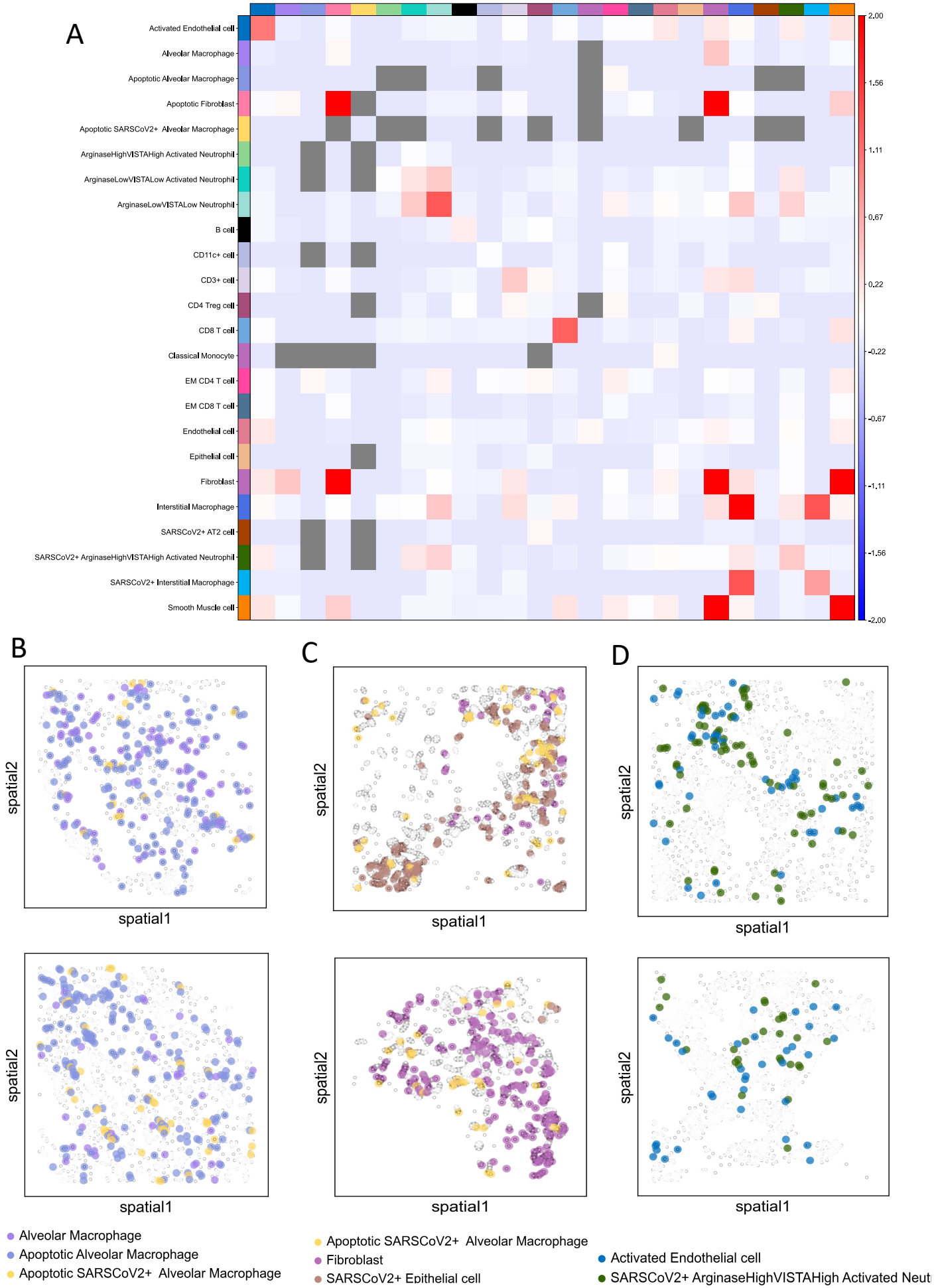

Extended data Table 1

	Case	Diagnosis	HIV	Sex	Age (yr)	PMI (hr)	Obese/Maln.	Pre-morbidity	S.S to death	Lung sc/sn	Nasal sc	Blood sc	Lung IMC	Nasal Lx	Blood Lx
Covid-19	3	C19	1	M	55-60	9	↑	DM2, HT	7		●	●	●	●	●
	5	C19	1	M	55-61	5	↑↑	DM2, HT	6				●		●
	6	C19	1	M	50-55	4	↑↑	DM2, HT	7	●		●	●	●	●
	7	C19	1	F	50-55	5	↑↑↑	Cancer	4		●		●	●	●
	8	C19	1	F	45-50	6	↑↑↑	HT, A	8				●	●	●
	9	C19	0	F	50-55	5.5	↑↑	None	8				●	●	●
	12	Sepsis+C19	0	F	60-65	9	↓	None	29 (2)*	●	●	●	●	●	●
	13	C19	0	F	70-75	5.5	↑↑	DM2, HT	20	●	●		●	●	●
	15	C19	0	M	55-60	10.5	→	None	5	●	●	●	●	●	●
No LRTD	2	TB	1	M	45-50	9	↓↓	None	13	●		●			●
	16	B. Pneum.	0	F	60-65	2.5	→	HT	9				●	●	
LRTD	1	TB	1	F	50-55	3	→	None	17					●	●
	4	L. Cancer	1	F	60-65	3	↓↓↓	None	10	●	●		●	●	●
	10	B. Pneum.	0	M	60-65	9.5	↓	HT	5	●	●	●	●	●	●
	11	Sepsis	1	F	50-55	10.5	↓↓	None	4				●	●	
	14	Stroke	0	F	50-55	9	→	None	2	●	●	●	●	●	●